



Carbon Dioxide Removal via Macroalgae Open-ocean Mariculture and Sinking: An Earth System Modeling Study

Jiajun Wu¹, David P. Keller¹, and Andreas Oschlies^{1,2}

¹GEOMAR Helmholtz Centre for Ocean Research Kiel, Kiel, Germany

²Kiel University, Germany

Correspondence: Jiajun Wu (jwu@geomar.de)

Abstract. In this study we investigate macroalgae open-ocean mariculture and sinking (MOS) as ocean-based carbon dioxide removal (CDR) method. Embedding a macroalgae model into an Earth system model, we simulate macroalgae mariculture in the open-ocean surface layer followed by fast sinking of the carbon-rich macroalgal biomass to the deep seafloor (depth >3,000m). We also test the combination of MOS with artificial upwelling (AU), which fertilizes the macroalgae by pumping nutrient-rich deeper water to the surface. The simulations are done under RCP4.5, a moderate emission pathway. When deployed globally between years 2020 and 2100, the simulated CDR potential of MOS is 270 PgC, which is further boosted by AU to 447 PgC. More than half of MOS-sequestered carbon retains in the ocean after cessation at year 2100 until year 3000.

The major side effect of MOS on pelagic ecosystems is the reduction of phytoplankton net primary production (PNPP) due to canopy shading and the competition for nutrients by macroalgae. MOS shrinks the mid layer oxygen minimum zones (OMZs) by reducing the organic matter export to, and remineralization in, subsurface and intermediate waters, while it creates new OMZs on the seafloor by oxygen consumption from remineralization of sunk biomass. MOS also impacts the global carbon cycle, reduces the atmospheric and terrestrial carbon reservoir when enhancing the ocean carbon reservoir. MOS also enriches the dissolved inorganic carbon in the deep ocean. Effects are mostly reversible after cessation of MOS, though recovery is not complete by year 3000. In a sensitivity experiment without remineralization of sunk MOS biomass, the entire MOS-captured carbon is permanently stored in the ocean, but the lack of remineralized nutrients causes a long-term nutrient decline in the surface layers and thus reduces PNPP.

Our results suggest that MOS has a considerable potential as an ocean-based CDR method. However, MOS has inherent side effects on marine ecosystems and biogeochemistry, which will require a careful evaluation beyond this first idealised modeling study.

20 1 Introduction

Anthropogenic emissions are rapidly increasing the global atmospheric CO₂ concentration. In the last decade (2011 to 2020), global fossil CO₂ emissions averaged $\sim 9.49 \text{ PgC yr}^{-1}$ (equivalent $\sim 34.8 \text{ PgCO}_2 \text{ yr}^{-1}$) with a growth rate of 0.4 \% yr^{-1} (Friedlingstein et al., 2021). In 2019, CO₂ emissions reached a record high of $9.71 \pm 0.49 \text{ PgC yr}^{-1}$ (equivalent $35.6 \pm 1.8 \text{ PgCO}_2 \text{ yr}^{-1}$), and there is no sign of a peak (Edo et al., 2019; Friedlingstein et al., 2021). The slow speed of emission reductions



25 until now makes it difficult to reach the promised climate goals to keep global warming within the guardrail of 2°C (Peters et al., 2013), much less the recent agreement to seriously consider an even more ambitious 1.5°C goal (UNFCCC, 2015).

In addition to mitigation efforts to reduce greenhouse gas (GHG) emissions, it is increasingly realized that Carbon Dioxide Removal (CDR), sometimes also called Negative Emissions Technologies (NETs), are likely to be a necessary step to achieve the targets of the Paris Agreement (Minx et al., 2017; Rogelj et al., 2018). CDR aim to remove GHGs, mainly CO₂, from
30 the atmosphere and store them, ideally permanently, in either the terrestrial, marine or geological carbon reservoirs, thereby mitigating global warming (Glaser, 2010). Due to the limited remaining emission budget (650 ± 130 Pg CO₂ to 1.5 °C and 1300 ± 130 Pg CO₂ to 2 °C), deployment of CDR is required in most pathways studied in the scientific literature to achieve these ambitious targets (Lawrence et al., 2018; IPCC, 2018).

As the second-largest inorganic carbon reservoir on the planet, the ocean plays a pivotal role in naturally regulating the
35 atmospheric CO₂ concentration. Since the beginning of the industrial era, the ocean has taken up more than 560 PgCO₂, about 25% of the anthropogenic CO₂ emissions (~2030 PgCO₂, Gruber et al. (2019); Ciais et al. (2013); Heinze et al. (2015)). Its high carbon storage capacity could theoretically match or exceed fossil fuel resources (Scott et al., 2015). Thus, a variety of ocean-based CDR methods have been proposed to take advantage of this potential storage capacity. The proposed ocean-based CDR approaches aim at increasing the rate of oceanic CO₂ uptake and storage by either enhancing abiotic processes (i.e.,
40 chemical or physical, e.g. ocean alkalization (Keller et al., 2014; Taylor et al., 2016; Köhler et al., 2013; Albright et al., 2016)) or biotic processes (e.g. ocean fertilization (Keller et al., 2014; Smetacek et al., 2012; Oschlies et al., 2010; Matear and Elliott, 2004; Robinson et al., 2014)). Some technologies also seek to remove CO₂ directly from seawater and store it in some other reservoir, e.g., a geological one (Eisaman et al., 2012).

Macroalgae species (also known as ‘seaweed’ or ‘kelp’) are highly efficient primary producers with a general net primary
45 production (NPP) rate of 91–522 gC m²yr⁻¹ and a high C:N ratio (Atkinson and Smith, 1983; Fernand et al., 2017). Utilizing macroalgae for biological ocean-based CDR has recently received a renewed interest (Duarte et al., 2017; Chung et al., 2011; Gao et al., 2020; Fernand et al., 2017; Raven, 2018). The macroalgae aquaculture industry is well established globally with an annual harvest of over 30 million tonnes wet weight (WW, FAO (2018)). Thus, some proposals have focused on using harvested macroalgae for producing biochar (Roberts et al., 2015; Bird et al., 2011) or bio-energy combined with carbon capture and
50 storage (BECCS, Chung et al. (2011); Buschmann et al. (2017); Gao and McKinley (1994); Chen et al. (2015); Fernand et al. (2017)). However, as current macroalgae aquaculture facilities are mainly located in coastal regions, the scope to expand macroalgae aquaculture is limited by the shortage of suitable coastal areas due to nutrient availability and shifting temperature regimes (Duarte et al., 2017; Oyinlola et al., 2020). To address these issues, several offshore macroalgae aquaculture facilities have been designed and evaluated (e.g. the SeaweedPaddock by Sherman et al. (2019), the offshore ring by Buck and Buchholz
55 (2004), or the depth-cycling strategy by Navarrete et al. (2021) in which macroalgae are physically towed into the deep nutrient-rich water at night). Moreover, the Advanced Research Projects Agency-Energy (ARPA-E) of the U.S. Department of Energy has committed more than 60 million dollars on the Macroalgae Research Inspiring Novel Energy Resources (MARINER) program to develop the technologies for macroalgal biomass production, including integrated ocean cultivation and harvesting

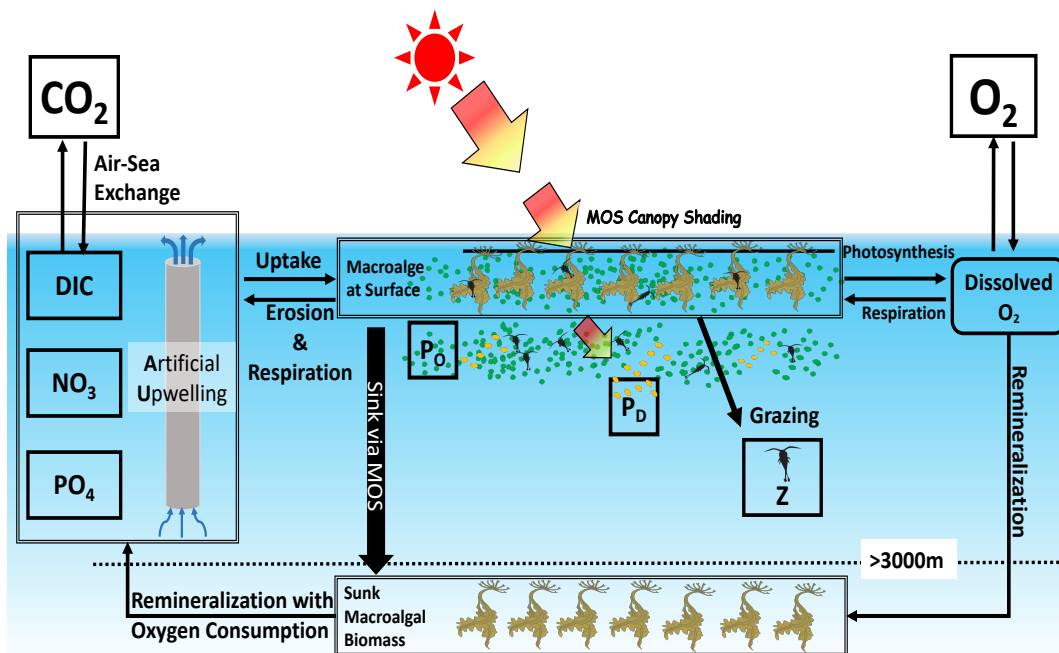


Figure 1. Schematic illustrating the biogeochemical fluxes and physical impacts of MOS on nutrients (NO_3 & PO_4), oxygen, dissolved inorganic carbon (DIC), ordinary phytoplankton (P_O in green), diazotrophs (P_D in pale brown) & zooplankton (Z).

systems (APAR-e, 2021). Thus, the ideas of expanding macroalgae cultivation to the open oceans (mariculture) are ambitious
 60 but no longer fictional, and they provide a theoretical possibility to expand macroalgae aquaculture to the open-ocean for CDR.

In this study we evaluate ‘Macroalgae Open-ocean mariculture and Sinking (MOS)’ as ocean-based CDR method that is
 designed to artificially enhance the macroalgae-based carbon dioxide removal. Simulated macroalgae are seeded and cultivated
 on offshore floating platforms that are moored to the seabed (e.g., see platform designs in Buck and Buchholz (2004)). The
 platforms are also assumed to float below the open ocean surface (at 5m depth) to avoid storm damages. At the end of an
 65 annual cycle, platforms with matured macroalgae are rapidly sunk to the seafloor and unload the biomass there. This can be
 thought of as a short circuiting of the biological pump by bringing marine biomass directly to the seafloor without having it
 remineralized along the way. Afterwards, the sunk biomass is assumed to continue remineralization at the seafloor, consuming
 oxygen and releasing dissolved inorganic carbon (C), nitrogen (N) and phosphate (P) into the deep ocean where it ideally
 remains for centuries to millennia (Fig.1). In practice, some of the biomass may also be permanently buried in sediments
 70 (Luo et al., 2019; Sichert et al., 2020), and we will explore the extreme case of zero remineralization in the water column in
 a sensitivity experiment. In another sensitivity experiment we investigate combining MOS with artificial upwelling (AU) to
 alleviate nutrient limitation in the open ocean surface (Duarte et al., 2017; Kim et al., 2019; Laurens et al., 2020).

To investigate the biogeochemical and climatic implications of MOS we use an Earth system model of intermediate com-
 plexity. Though the idea of massive macroalgae cultivation and biomass offsetting for CDR has been assessed in some earlier



75 publications (Orr and Sarmiento, 1992; Gao and McKinley, 1994; Froehlich et al., 2019; Lehahn et al., 2016), as far as we
are aware it has not been evaluated using an Earth system model (ESM). ESM-based assessments are required for studying
the response of the global carbon cycle to such perturbations and for comprehensively estimating the efficacy (with regards
to atmospheric CO₂ removal) of such methods. Furthermore, such models can dynamically simulate macroalgae growth, the
permanence of carbon storage (i.e., the fate of sunk biomass on the seafloor), as well as their interactions with global marine
80 biogeochemistry. It is essential to clarify these issues before any decisions about eventual implementation of MOS can be
made.

2 Methods

2.1 Model description

In this study we employ the University of Victoria Earth System Climate Model (UVic ESCM) version 2.9 (Weaver et al.
85 (2001); Eby et al. (2009); Keller et al. (2012)), which consists of three dynamically coupled components: a three-dimensional
ocean circulation model (Pacanowski, 1996) including a dynamic–thermodynamic sea-ice model (Bitz and Lipscomb, 1999),
a terrestrial model (Meissner et al., 2003; Weaver et al., 2001) and a simple one-layer atmospheric energy–moisture balance
model (Fanning and Weaver, 1996). The model has a fully coupled carbon cycle including dynamic terrestrial, atmospheric
and oceanic carbon inventories. The horizontal resolution of all components is 3.6° longitude × 1.8° latitude, and the ocean
90 component has 19 vertical layers. The descriptions of air–sea gas exchange and seawater carbonate chemistry are based on the
Ocean Carbon Cycle Model Intercomparison Project (OCMIP) abiotic protocol (Orr et al., 1999). The ocean biogeochemistry
is presented with a nutrients–phytoplankton–zooplankton–detritus (NPZD) model that includes one general phytoplankton,
diazotrophs, and one zooplankton type (Keller et al., 2012; Eby et al., 2013). The UVic ESCM has been evaluated in several
recent studies (e.g. Keller et al. (2014); Mengis et al. (2016); Reith et al. (2016); Kvale et al. (2021)).

95 2.2 Modelling MOS in the UVic ESCM

2.2.1 Macroalgae model

The macroalgae model is an idealized generic model of genus *Laminaria* and *Saccharina*, mainly based on Martins and
Marques (2002) and Zhang et al. (2016). For simplicity and to limit the number of state variables, we did not include a
dynamic C:N:P ratio or a representation of luxury nutrient uptake and storage (Broch and Slagstad, 2012; Hadley et al., 2015).
100 The assumed constant C:N:P ratio (Tab.1) is based on seasonally averaged measurements of the biomass composition of
these genus (Zhang et al., 2016; Martins and Marques, 2002). Frond and macroalgae life cycle processes (e.g. alternations of
generations) are also not considered in our model (Brush and Nixon, 2010; Trancoso et al., 2005; Duarte and Ferreira, 1997).
We thus assume that the plantlet (e.g. sporophytes for *Saccharina*) will be reseeded annually on the MOS infrastructure. The
assumed deployment strategy, i.e., timing of seeding and sinking, of MOS is latitude-dependent according to the seasonality



105 of solar irradiance (see Sect.3.1). Whenever conditions are unfavorable for macroalgae and no growth occurs during an annual cycle, no re-seeding of macroalgae will occur in these regions.

The growth of macroalgae is regulated by water temperature (**T**), solar irradiance (**I**) and dissolved nutrient concentrations. The rate of biomass change is governed by Eq. 1 as the imbalance of **NGR** (net growth rate, d^{-1}) and **LR** (loss rate, fraction of daily biomass loss due to mortality, erosion and grazing by zooplankton, d^{-1}).

$$110 \quad \frac{dBiomass}{dt} = (NGR - LR) \times Biomass \quad (1)$$

The NGR is regulated by:

$$NGR = R_{growth} - R_{resp} \quad (2)$$

where R_{growth} is the gross growth rate (d^{-1}) and R_{resp} is the respiration rate (d^{-1}). R_{growth} is a function with limiting factors of sea water temperature (T_w), irradiance (I_{ma}) and external nutrient concentrations (NO_3 and PO_4 , **NP**).

$$115 \quad R_{growth} = \mu_{max} \times f(T_w) \times f(NP) \times f(I_{ma}) \quad (3)$$

In the current model the macroalgal growth rates are controlled by external concentrations of available nutrients via assumed Michaelis-Menten kinetics with half-saturation constants K_N and K_P for NO_3 and PO_4 , respectively:

$$f(N) = \frac{NO_3}{K_N + NO_3} \quad (4)$$

$$f(P) = \frac{PO_4}{K_P + PO_4} \quad (5)$$

$$120 \quad f(NP) = \text{Min}\{f(N), f(P)\} \quad (6)$$

The temperature limiting factor used here is an optimum curve following Bowie et al. (1985). T_{opt} is the species-specific optimum temperature at which the growth rate is maximized.

$$f(T_w) = e^{-2.3 \times X_T^2} \quad (7)$$

$$X_T = \frac{T_w - T_{opt}}{T_x - T_{opt}} \quad (8)$$

$$125 \quad T_x = \begin{cases} T_{min} & \text{if } T_w \leq T_{opt} \\ T_{max} & \text{if } T_w > T_{opt} \end{cases} \quad (9)$$



Respiration is described by an Arrhenius function considering water temperature T_w in degrees Celsius (Duarte and Ferreira, 1997; Martins and Marques, 2002):

$$R_{resp} = R_{max20} \times r^{(T_w - 20)} \quad (10)$$

where R_{max20} is the maximum respiration rate at 20 °C of the simulated macroalgae species, r stands for the empirical coefficient for macroalgae respiration (Tab. 1).

Solar irradiance density is another limiting factor for macroalgae photosynthesis. Similar to Schmittner et al. (2005) and Keller et al. (2012), here we employ Steele's photo-inhibition relationship (Kirk, 1994) to describe the limiting factor of shortwave radiation ($f(I_{ma})$) at depth Z , which describes the distance between the ocean surface and the top of the macroalgae meadow (Eq.11). In the UVic ESCM, the shortwave radiation (I_{ma}) reaching the depth Z is calculated with Eq.12 modified from Keller et al. (2012) and Schmittner et al. (2005). I_s stands for the shortwave radiation density at the top of the layer. P_O and P_D are biomass of ordinary phytoplankton and diazotrophs, respectively, in the layers above the macroalgae meadow. k_w is the light attenuation coefficient for water. I_{opt} is the optimum light intensity for macroalgae growth. k_c is the light attenuation coefficient of phytoplankton and also accounts for co-varying particulate and dissolved inorganic and organic materials (Kvale and Meissner, 2017). As described in Sect.2.2.1, the morphology of the frond will not be considered, therefore the self-shading effects by fronds are not considered here (Duarte and Ferreira, 1997; Brush and Nixon, 2010).

$$f(I_{ma}) = \frac{I_{ma}}{I_{opt}} \times e^{(1 - \frac{I_{ma}}{I_{opt}})} \quad (11)$$

$$I_{ma} = I_s \times e^{(-k_w Z_m - \int_0^{Z_m} (P_o + P_D) k_c \times dZ_m)} \times df \quad (12)$$

with Z_m denoting the depth of MOS macroalgae platforms beneath the water surface. Z_m is assumed as 5 meters, compromising the empirical depth with sufficient light for macroalgae photosynthesis (1m to 2m for cultivation (Buck and Buchholz, 2004), 0m to 10m for wild communities (Eriksson and Bergström, 2005)) and the depth to reduce the risks of damaging by stressful turbulence or severe weather events (e.g. hurricanes). df denotes the day length as a fraction of 24 h.

The loss rate LR is regulated by:

$$LR = ER + Graze_{ma} \quad (13)$$

$$ER = Biomass \times R_{erosion} \quad (14)$$

$$Graze_{ma} = \mu_Z^{max} Z \times \psi_{ma} \times Biomass \quad (15)$$

where the erosion of biomass (ER) is controlled by the individual erosion rate $R_{erosion}$ which is a constant independent of physical impacts according to Trancoso et al. (2005) due to the absence of a dynamic frond morphology function. The eroded macroalgal biomass will be directly converted back to nutrients and DIC (dissolved inorganic carbon) according to the macroalgae stoichiometry ratios without remineralization or further degradation by zooplankton. $Graze_{ma}$ is the biomass loss



155 due to grazing by zooplankton. Z is the zooplankton biomass which is calculated by the NPZD model. μ^{max}_Z stands for the maximum potential growth rate of zooplankton defined in Keller et al. (2012, Eq.28). The zooplankton grazing preference on macroalgae (ψ_{ma}) is defined in Sect.2.2.3.

2.2.2 Remineralization of sunk macroalgal biomass

160 Biomass sinking is simulated by instantly transferring the macroalgal biomass from the surface grid cell to the deepest grid cell at the respective location at the end of each cultivating period. Afterwards the next macroalgae generation will start to grow in the surface layer. Eq.(16) calculates the temperature dependent remineralization rate of sunk macroalgal biomass (μ_{ma}) following the function of remineralization of detritus in the UVic ESCM (described in Schmittner et al. (2008, Eq.A16)). Remineralization consumes oxygen and returns DIC, PO_4 and NO_3 from the sunk macroalgal biomass to the sea water, and is described as

$$165 \mu_{ma} = \mu_{ma0} \exp(T_w/T_b)[0.65 + 0.35 \tanh(O_2 - 6)] \quad (16)$$

where μ_{ma0} is the remineralization rate of sunk macroalgal biomass at 0°C . T_w and T_b represent the sea water temperature and e-folding temperature of biological rates, O_2 is the dissolved oxygen concentration in mmol m^{-3} . When the dissolved oxygen is insufficient ($< 5 \text{ mmol m}^{-3}$), aerobic remineralization will be replaced by oxygen-equivalent, but slower, denitrification via reduction of NO_3 (Keller et al., 2012). Note that remineralization will cease when NO_3 is completely consumed.

170 There are considerable uncertainties concerning the fate of sunk macroalgae (Sichert et al., 2020; Krause-Jensen and Duarte, 2016; Luo et al., 2019). A sensitivity simulation explores the situation where μ_{ma0} is set to zero, which would assume permanent deposition of the sunk biomass on the seafloor without decaying.(Sect.3.2).

2.2.3 Interactions with pelagic microbial ecosystems

175 Besides the competition for nutrient resources, the macroalgae canopies may also reduce downward solar irradiance ('canopy shading') and thus limit phytoplankton photosynthesis beneath the macroalgae (Jiang et al., 2020)). Furthermore, zooplankton can graze on macroalgae (Baird et al., 2003). Eq.(17, modified from Eq.14, (Keller et al., 2012)) describes the shortwave radiation attenuation (I_{phyt}) through the macroalgae layer as well as phytoplankton and water (MOS is not deployed in areas covered by sea ice):

$$I_{phyt} = I_s \times e^{-k_w Z - \int_0^Z (P_o + P_D) k_c \times dZ - k_{ma} \times h_{ma} \times Biomass} \quad (17)$$

180 where k_{ma} , the macroalgae light extinction coefficient (m^{-1}), is calculated based on the biomass of macroalgae in carbon as:

$$k_{ma} = a_{ma} \times Biomass \times MR_{C:N} \quad (18)$$

Here a_{ma} is the macroalgae carbon specific shading area ($\text{m}^2 \text{ kgC}^{-1}$, Trancoso et al. (2005)), h_{ma} is the thickness of macroalgae layer, $MR_{C:N}$ stands for the molar C:N ratio of macroalgal biomass.



The original NPZD model in Keller et al. (2012) is extended by allowing zooplankton to graze on macroalgae. The grazing
185 preference for macroalgae (ψ_{ma}) is set to 1×10^{-4} according to observational studies (Trancoso et al., 2005). Macroalgae
thus provide a grazing option for zooplankton in addition to the traditional NPZD-type model food sources (phytoplankton,
diazotrophs, detritus and zooplankton via self-grazing). Therefore, the four original grazing preferences (0.3 on phytoplankton,
0.1 on diazotrophs, 0.3 on detritus and 0.3 on zooplankton (Keller et al., 2012, Tab.1)) are reduced by $\frac{1}{4} \psi_{ma}$ each. In the areas
where MOS are absent (i.e, in the ice-covered ocean surface), the zooplankton grazing will follow the original description
190 in Keller et al. (2012, Tab. 1) without the preference for macroalgae. No CaCO_3 formation by macroalgae is simulated here
(Bach et al., 2021; Macreadie et al., 2017, 2019), as calcareous macroalgae species and epibiont calcifiers are not considered.
Therefore, the only alkalinity impact of growing and remineralizing macroalgae comes via changes in nitrate and phosphate.

2.2.4 Mass conversions

In order to parameterize and validate the model, it is necessary to convert from commonly measured macroalgae variables (often
195 in wet and dry weight units) to the model units. These conversions include: the calculation of carbon and CO_2 sequestered in
macroalgal biomass (C_{ma} , gram carbon), as well as the conversions of dry weight (DW, gram) and wet weight (WW, gram)):

$$C_{ma} = \text{Biomass} \times MR_{C:N} \times 12.011 \quad (19)$$

$$\text{CO}_{2ma} = C_{ma} \times 3.67 \quad (20)$$

$$DW = C_{ma} \div MR_{C:DW} \quad (21)$$

200 $WW = DW \times MR_{DW:WW} \quad (22)$

where 3.67 is the ratio between the atomic mass of CO_2 (44 g/mol) to carbon (12g/mol), *Biomass* is in moles of nitrogen,
12.011 is the relative molecular weight of carbon (g/mol).

2.2.5 MOS carbon retained in the ocean and outgassing

The DIC from remineralization of sunk biomass will eventually be conveyed back to the ocean surface and may leak back to
205 the atmosphere. Eq.23 calculates the ocean-retained fraction (FR, %) of MOS-captured carbon (MOS-C).

$$FR = \frac{C_{retained}}{C_{captured}} = \frac{(\text{DIC}_{remineralized} + C_{SunkBiomass})}{C_{captured}} \quad (23)$$

where the $C_{captured}$ is carbon in cumulative sunk biomass, $C_{SunkBiomass}$ is the sunk macroalgal biomass that still remains on
the sea floor.

In order to track the leakage of MOS-C after remineralization, a tracer of remineralized MOS-C (MOS_DIC) is added to
210 the UVic ESCM aside of the original DIC tracer. MOS_DIC participates in the inorganic ocean carbon cycle Weaver et al.
(2001, Section 3e). When reaching the surface, the outgassing of MOS_DIC will follow the air-sea gas exchange process in
UVic ESCM, which is given in Weaver et al. (2001, Section 3e). To assess its outgassing, we calculate the partial pressures of



CO₂ (pCO₂) in the ocean for MOS_DIC separately. The air-sea exchange flux of MOS-C is also calculated for analysing the location and quantity of outgassing. The results of MOS-C outgassing is shown in Sect. 4.6.

Table 1. Model parameters

Symbol	Parameter	Unit	Value	Reference
a_{ma}	Macroalgae carbon specific shading area	$m^2 kg C^{-1}$	11.1	108
d	Distance between the cultivating ropes	m	10	111
$R_{erosion}$	Individual erosion rate	$\% d^{-1}$	0.01	115
I_{opt}	Optimum light intensity for macroalgae growth	$W m^{-2}$	180	115
NO_3	Nitrate Concentration	$\mu mol l^{-1}$	model calculation	50
PO_4	Phosphate Concentration	$\mu mol l^{-1}$	model calculation	50
K_N	Half-saturation constant for nitrogen uptake	$\mu mol l^{-1}$	2	115
K_P	Half-saturation constant for phosphorus uptake	$\mu mol l^{-1}$	0.1	115
k_w	Coefficient of light attenuation through water	m^{-1}	0.04	50
k_c	Coefficient of light attenuation through phytoplankton	$m^{-1}(mmol m^{-3})$	0.047	50
M_{ma}	Thickness of MOS macroalgae canopy	m	10	109
$MR_{C:N}$	Molar C:N ratio of macroalgal biomass	-	20	5
$MR_{P:N}$	Molar P:N ratio of macroalgal biomass	-	0.1	5
$MR_{C:P}$	Molar C:P ratio of macroalgal biomass	-	111	calculated
$MR_{DW:WW}$	Ratio of DW to WW of macroalgal biomass	-	0.1 (values reported:0.05~0.2)	2; 22; 111
$MR_{C:DW}$	Carbon content of dried macroalgal biomass	$\%$	30	20
$MR_{N:DW}$	Nitrogen content of dried macroalgal biomass	-	0.16	28
R_{max20}	Maximum respiration rate at 20°C	$\% d^{-1}$	1.5	70; 115
r	Empirical coefficient for macroalgae respiration	d^{-1}	1.047	70
Seed	Initial macroalgal biomass per kilometer cultivating line	$kg C km^{-1}$	2.5	111
T_b	E-folding temperature of biological rates	$^{\circ}C$	15.56	97
T_{opt}	Optimum temperature for growth	$^{\circ}C$	20	12
T_{max}	Upper temperature limit above which growth ceases	$^{\circ}C$	35	13
T_{min}	Bottom temperature limit below which growth ceases	$^{\circ}C$	0	70
u_{max}	Maximum growth rate	d^{-1}	0.2	115
w	Areal mean artificial upwelling rate	$cm d^{-1}$	1,10	82
Y_{max}	Maximum yield of macroalgal biomass on MOS	$t DW km^{-2} yr^{-1}$	3300	
ψ_{ma}	Zooplankton grazing preference on macroalgae	-	1×10^{-4}	108
μ_{ma0}	Remineralization rate of sunk macroalgal biomass at 0 °C	$\% d^{-1}$	7	86

215 3 Experiment design

The UVic ESCM is spun up for > 10,000 years to an equilibrium state under pre-industrial (year 1765) atmospheric and astronomical boundary conditions, and is then integrated for another 250 years without prescribing atmospheric CO₂ concentrations to allow the carbon cycle to equilibrate. Afterwards, the model is run from 1765 until 2005 and forced with historical fossil-fuel emissions and land-use changes (crop and pastureland) (Keller et al., 2014). From year 2005 to 2100, simulations are forced



220 with CO₂ emissions and other non-CO₂ GHGs, land use change by agriculture, volcanic radiative forcing and sulphate aerosols
which are prescribed according to the Representative Concentration Pathway 4.5 (RCP4.5, Meinshausen et al. (2011); Thomas
(2014); Keller et al. (2014); Partanen et al. (2016). Solar insolation at the top of the atmosphere, wind stress, and wind fields are
varied seasonally. After the year 2300, CO₂ are assumed to decrease linearly until the end of year 3000 with the other forcing
held constant.

225 The full list of simulations is given in Table 3. To test the maximum potential as well as the global carbon cycle and
biogeochemical responses, we simulate MOS for 1,000 years beginning in year 2020 (MOS_Conti). Additionally, termination
experiments (MOS_Stop) are performed to analyse the response of the ocean and climate to an abrupt termination of MOS.

3.1 Deployment strategies of MOS

The current study focuses on estimating the maximum carbon sequestration potential of MOS, and assumes instantaneous
230 seeding on floating infrastructure in the open ocean. The macroalgae is represented as a biogeochemical tracer (Eq 1) that is
not subject to physical transports and remains fixed in the top (1st) ocean layer of the UVic ESCM, which is assumed to be
well mixed. MOS deployment must fulfill the following requirements:

- the water depth must be $\geq 3,000\text{m}$: according to the assessment by Reith et al. (2016), leakage of dissolved inorganic carbon
235 added to deep waters (in this case from remineralization of sunk macroalgal biomass) is small at such depths compared
to shallower ones;
- the ambient surface NO₃ concentration is greater than *Seed* plus K_N (Tab. 1); this ensures sufficient nutrients for initial
growth as *Seed* is directly transferred from dissolved NO₃ and K_N is the half saturation constant for NO₃ uptake;
- spatially located between 57°N and 72°S to remain in sea ice free waters.

Note that the DIC, N and P components of the initial *Seed* are directly removed from the inorganic matter pool of the respective
240 grid box in order to maintain model mass balance and avoid adding extra nutrients/carbon to the ocean at the time of seeding.

During the MOS simulations, seasonality of temperature as well as solar radiation are essential limiting factors of the primary
productivity of MOS in various latitudinal regions. In order to avoid the unnecessary loss of macroalgal biomass during winter
periods when solar radiation is insufficient and the ambient water temperature is low, we partitioned the global ocean surface
into three belts (N, M and S) and pragmatically applied farming strategies according to Tab. 2.



Table 2. Latitudinal division of MOS deployment regions

Belt	Latitudinal range	Date for	
		Seeding	Sinking
N	51.3°N to 17.1°N	01.May	31.Oct
M	17.1°N to 18.9°S	01.Jan	31.Dec
S	18.9°S to 56.7°S	01.Nov	30.Apr*

*In the following year

245 The maximum yield of *Biomass* is set to a constant value of Y_{max} (Tab.1). When the biomass reaches Y_{max} in a grid cell, macroalgae will stop growing and wait for sinking. After an annual cultivation cycle, the macroalgal biomass is instantaneously delivered to the seafloor apart from a small fraction (equivalent to *Seed*) that remains at the surface for re-seeding. In some regions where conditions are unfavorable and no net macroalgae growth had occurred during the last cultivation period, the total *Biomass* will be sunk once without any further re-seeding. In order to prevent MOS from removing too much atmospheric
250 CO₂ in long-term simulations where emissions eventually reach zero, MOS deployment will be terminated once atmospheric CO₂ concentration hit 280ppm, assuming that there is no need for more CDR once pre-industrial CO₂ values have been reached.

3.2 Sensitivity Studies

As test simulations indicated that the CDR potential of MOS is in many ocean regions limited by the availability of nutrients in the surface layer, sensitivity simulations were performed with MOS combined with artificial upwelling (AU) that pumps up
255 nutrient-rich deeper waters to the surface and thereby relaxes nutrient stress and enhances the macroalgae growth.

The simulated MOS-AU system is based on Oschlies et al. (2010) and Keller et al. (2014). However, because these earlier studies revealed a dominant effect associated with low temperatures of the upwelled colder waters, we here concentrate on the nutrient aspect and simulate a hypothetical MOS-AU system that keeps temperatures at ambient levels (e.g. via heat exchangers).

260 In the simulated AU system, water together with dissolved tracers is transferred from the grid box at the lower end of the pipes to the surface grid box resulting in a model grid box-average upwelling rate (w , set to 1cm/day). The lower end of the pipes is fixed at a depth of 1000m. Similar to the normal MOS simulations without AU, the MOS_AU simulations are deployed from year 2020 and then terminated at either year 2100 in discontinuous run or year 3000 in continuous one (Tab. 3).

The MOS-AU joint system is deployed using the following strategies: AU pipes will be deployed everywhere with depth \geq
265 3000m and start upwelling immediately. If surface nutrient concentrations are raised to the initial seeding condition (Sect. 3.1) in any grid box, MOS will be deployed, thereby expanding the range where MOS can grow.

Another model parameter selected for sensitivity studies is the remineralization rate of sunk macroalgal biomass (μ_{ma} , Eq. 16). μ_{ma} is a critical factor impacting the residence time of MOS-captured carbon in the ocean and associated benthic oxygen



consumption by remineralization. Macroalgal biomass has been reported to be recalcitrant to microbial degradation, however, the fate of macroalgal biomass in the deep sea is uncertain (Krause-Jensen and Duarte, 2016; Luo et al., 2019; Sichert et al., 2020). Thus, an extreme and idealized situation with μ_{ma} set to zero is tested in sensitivity simulations (MOS_NoRe). This can be thought of as a case where all biomass is permanently buried upon reaching the seafloor.

Table 3. Description of the Model Experiments. "Stop" represents the termination of the simulation in year 2100; "Conti" represents the continuous MOS deployment till year 3000; "AU" represents artificial upwelling; NoRe represents zero-remineralization of sunk macroalgal biomass.

Category	Experiment	Description
Normal MOS simulations	Control_RCP4.5	Control simulation under RCP4.5
	MOS_Conti	As Control_RCP4.5, but MOS deployed from year 2020 to year 3000
	MOS_Stop	As Control_RCP4.5, but MOS implemented from year 2020 to year 2100
Sensitivity simulations	MOS_Conti_NoRe	As MOS_Conti, but with zero remineralization rate
	MOS_Stop_NoRe	As MOS_Stop, but with zero remineralization rate
	MOS_AU_Conti	MOS synergy with AU, area-averaged upwelling velocity(w) is 1cm/day.
	MOS_AU_Stop	As MOS_AU_Conti, but MOS implemented until year 2100

4 Results

4.1 Evaluation of MOS

To evaluate if the simulated MOS systems have plausible macroalgae growth characteristics, we evaluate the seasonal dynamics of the simulated MOS system for a 30 days averaged time slice from 2020 to 2024 under the RCP4.5 emission scenario and without artificial upwelling.

4.1.1 Distribution of MOS

The red contours in Fig.2a delineate the occupied area that basically follows the pattern of the simulated NO_3 -rich ocean surface (Keller et al. (2012, Fig 9), Garcia et al. (2010, WOA2009 Dataset)) in the Northern and the equatorial Eastern Pacific, as well the Southern Ocean. Except for the coastal regions and Arctic areas which are not considered for MOS here, the distribution pattern of MOS agrees with the other estimation of potential open-ocean macroalgae farming locations (e.g. Lehahn et al. (2016, Fig.2.A), Froehlich et al. (2019, Figure 1.)). Another powerful limiting factor is the ocean surface temperature (Garcia et al., 2010, WOA2009 Dataset) which is too warm in many places for our idealized species, i.e., temperatures are above the T_{opt} (20°C) and nearly reaches the T_{max} (35°C).

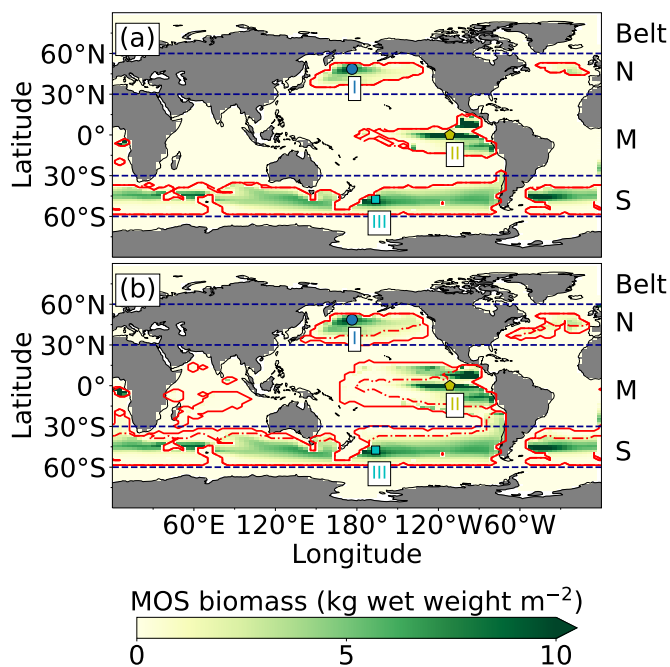


Figure 2. Annual vertically integrated NPP of MOS (a) and MOS_AU (b) in year 2024. Red solid lines outlines the MOS occupied area at year 2024 in both, while red dashed lines outline the initial MOS seeding area at year 2020 in (a). The simulated MOS area generally covers the NO_3 -rich ocean surface (a) and can be expanded with nutrients supplement by AU (b), larger than the estimated adequate area for macroalgae in previous studies (Lehahn et al., 2016; Froehlich et al., 2019)). Results for areas I (blued circle), II (yellowish pentagon) and III (cyan rectangle) are discussed in the text and displayed in Fig 3.

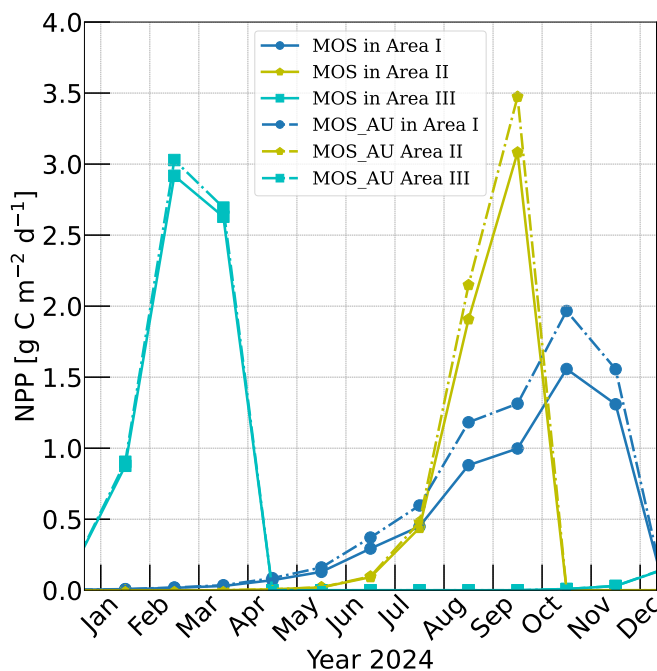


Figure 3. Vertically integrated MOS NPP rates simulated for year 2024 and representative Areas I (dark blue circle), II (yellow pentagon) and III (cyan rectangle) highlighted by rectangles with corresponding colours in Fig.2. The NPP of MOS (solid) from the selected area I, II and III are reasonable compared to reported macroalgae NPP, and MOS_AU (dashed) shows an enhancement of NPP as expected.

At the beginning of year 2020, a surface area S_{MOS} of 72 million km^2 was selected by the MOS algorithm according to the requirements described in Sect.3. This is equivalent to a total cultivated rope length (L_{MOS}) of 7.2×10^9 km (Eq.A1, Sect.A1). When the macroalgae start to grow and to consume nutrients, regions with nutrient levels insufficient for further growth are gradually abandoned. By the end of year 2024, the MOS coverage has declined by about 3% to 69.6×10^9 km^2 (Tab.4).

290 Despite the similar distribution patterns, MOS occupied area (69.6×10^9 km^2 , $\sim 19.7\%$ of the world ocean) is larger than the assessments of $\sim 10\%$ of the world ocean by Lehahn et al. (2016) and ~ 48 million km^2 by Froehlich et al. (2019). Compared to the static estimation based on historical nutrient levels and temperature suitability (Lehahn et al. (2016, Fig.2.A)), the dynamic processes redistributing nutrients as well as the explicit macroalgae growth module in our simulations contribute to the simulated larger potential area for MOS, especially in equatorial Eastern Pacific and the Southern Ocean. Besides, the



295 adequate area for macroalgae cultivation was limited to the Economic Zones (EEZs) by Froehlich et al. (2019) due to limitations
of cost and political feasibility. This constraint has been ignored in the current study. Thus, our simulated MOS-adequate area
is 45% larger than the estimation by Froehlich et al. (2019).

4.1.2 Macroalgae model validation

Validation of the macroalgae model is crucial, as the productivity and macroalgal biomass yield is vital for CO₂ sequestration.
300 Here we examine the simulated seasonality, NPP rate, and biomass yield of MOS in comparison with available observations
and assessments. Simulated NPP is high in the first year of deployment in many regions because nutrients are abundant, and
then sharply declines in the following years as a new local biogeochemical state is reached. Thereafter, NPP gradually reaches
a relatively steady state by 2024 (Fig.A2). To provide some validation of the macroalgae model we select three areas named
Area I, II and III from Belt N, M and S (Fig.3) and analyse their performance in year 2024. Each area covers 4 grid boxes in
305 the uppermost ocean layer of the UVic ESCM.

In our simulations, simulated macroalgae NPP rates are comparable to the observed ranges in the productive areas that we
selected here. Observed wild macroalgae NPP varies widely, ranging from 91 to 750 gC m⁻² yr⁻¹ (Krause-Jensen and Duarte,
2016). Our model reproduces the macroalgae NPP of 159.2-199.3 gC m⁻² yr⁻¹ in the selected areas (Tab.4). Simulated
biomass yields in these areas are in the previously reported range as well. Reports of the biomass yield of aquacultured
310 *Laminaria saccharina* (now regarded as a synonym of *Saccharina latissima*) range from 40t DW km⁻² yr⁻¹ in an off-shore
cultivation experiment by Buck and Buchholz (2004) to 456t DW km⁻² in a coastal cultivation experiment by Peteiro et al.
(2014). In our simulations, the yield of selected areas ranges from 492.4 to 648.2t DW km⁻² yr⁻¹. The selected Area I yields
648.2 DW km⁻² yr⁻¹. In regions with similar latitudes as Area I, the biomass yield of aquacultured *Saccharina japonica*
(formerly classified as *Laminaria japonica*) was ~300t DW km⁻² yr⁻¹ in China (Zhang et al., 2016) and reached 7,280t
315 DW km⁻² yr⁻¹ in Japan (Yokoyama et al., 2007). Nevertheless, some simulated low values from the globally averaged and
latitudinal belt-averaged results are not surprising considering that the open ocean tends to be more nutrient limited than coastal
or near-shore regions where the aforesaid observed macroalgae NPP was measured. Our results provide some confidence that
our idealized model can simulate macroalgae well enough with respect to typical biomass yield, seasonality and geographical
distribution.



Table 4. Properties of globally implemented MOS. Selected areas are from data of year 2024, whereas Belt areas are values averaged from 2020 to 2024. Areal NPP rates and Biomass Yield refer to the respective MOS area.

Property	Unit	Exp.	Selected area(10^3 km^2)			Belt(10^9 km^2)			
			I	II	III	N	M	S	Global
MOS occupied area(S_{MOS})	km^2	MOS	218.8	320.3	204.2	9.1	15.7	44.8	69.6
		MOS_AU				17.4	44.3	64.6	126.3
NPP	$\text{gC m}^{-2} \text{ yr}^{-1}$	MOS	159.2	176.9	199.3	50.8	52.0	67.5	61.8
		MOS_AU	202.2	231.1	217.7	45.5	32.2	56.9	46.7
Biomass Yield	$\text{t DW m}^{-2} \text{ yr}^{-1}$	MOS	648.2	492.4	579.7	173.2	160.3	206	191.4
		MOS_AU	715.3	615.4	597.0	142.2	85.4	169	136
Total CO_2 captured in biomass	$\text{Pg CO}_2 \text{ yr}^{-1}$	MOS	0.14	0.16	0.12	1.6	2.5	9.2	13.3
		MOS_AU	0.15	0.20	0.12	2.5	3.8	10.9	17.2

320 4.2 Evaluation of MOS with Artificial Upwelling (AU)

As expected, AU increases the area occupied by MOS from $69.6 \times 10^9 \text{ km}^2$ in the run without AU to $129.6 \times 10^9 \text{ km}^2$ in the run with AU (Fig.2.2). Obvious expansions of areas with suitable growing conditions are found in the Eastern Tropical Pacific and the North Atlantic. AU also expands S_{MOS} to the Indian Ocean, which was almost abandoned in regular MOS simulations. In Area I, II and III, both NPP rate and biomass yield are enhanced due to the upwelled nutrients (column Belt, 325 Tab.4, Fig.3). A closer look into the Belt N, M and S areas shows that both the NPP rate and biomass yield per square-meter of the deployment area decrease in simulation MOS_AU when compared to the standard MOS simulation (column Belt, Tab.4). This is related to a 'dilution effect': in the new MOS-adequate areas increased by AU, the available nutrients are limited, thus the MOS NPP is relatively low compared to the original nutrient-rich NPP areas. Despite of this, the expanded MOS area in MOS_AU increases the total CO_2 captured by about $\sim 30\%$ (Tab.4).

330 4.3 MOS deployment until year 2100

This section showcases the CDR and climate change mitigation capacities of MOS within the 21st century. Impacts of MOS on marine biogeochemistry (nutrients, dissolved oxygen and pelagic ecosystem) and global carbon cycles will also be examined.

4.3.1 CDR & climate change mitigation capacities

Over the 80 years between year 2020 and year 2100, MOS is mainly deployed in nutrient-rich regions such as the Southern 335 Ocean and the northern and eastern equatorial Pacific (Fig.B1(a)), despite some contraction of initially occupied areas occurred due to the removal of nutrients.



By the year 2100, MOS (MOS_Stop and MOS_Conti) has sequestered 270 PgC (990 PgCO₂, Tab.5), representing ~37% of the cumulative CO₂ emissions in the RCP4.5 pathway. Essentially all of MOS-captured carbon is retained in the ocean over this period as either remineralized dissolved inorganic carbon, or organic carbon in the sunk biomass.

Table 5. Model Simulations under the RCP4.5 emission scenario. MOS-C represents the carbon sequestered via MOS. C_{atm} , C_{oc} , C_{ter} stand for atmospheric, oceanic and terrestrial carbon reservoir respectively. Δ SAT stands for surface averaged temperature relative to 13.18°C, the pre-industrial.

Experiment	pCO ₂ (ppm)		Cumulative CO ₂ Emission (PgC)		MOS-C (PgC)		FR (%)		C_{atm} (PgC)		C_{oc} (PgC)		C_{ter} (PgC)		Δ SAT (°C)		Phyt NPP ($\frac{PgC}{yr}$)		
	2100	3000	2020-2100	2020-3000	2020-2100	2020-3000	2100	3000	2100	3000	2100	3000	2100	3000	2100	3000	2100	3000	
Control_RCP4.5	573.1	615.5	718.1	1392	/	/	/	/	1217	1307	37611	38180	1854	1935	2.52	4.32	47.6	56.8	
<i>Normal MOS experiments minus Control_RCP4.5</i>																			
MOS_Conti	-67.2	-297.0	718.1	1392	270.0	2533	100	75.3	-142.6	-630.5	171.8	901.9	-29.7	-278.8	-0.38	-2.87	-9.5	-22.2	
MOS_Stop	-67.2	-28.5	718.1	1392	270.0	270.0	100	58.6	-142.6	-60.5	171.8	77.4	-29.7	-16.8	-0.38	-0.23	-9.5	-1.8	
<i>Sensitivity MOS experiments minus Control_RCP4.5</i>																			
MOS_AU_Conti	-108.7	-225.3	718.1	1392	446.8	1970	99.9	72.9	-230.7	-452.3	283.9	665.3	-53.2	-186.8	-0.63	-2.49	-5.1	-13.0	
MOS_AU_Stop	-108.7	-52.3	718.1	1392	446.8	446.8	99.9	64.4	-230.7	-111.1	283.9	143.5	-53.2	-32.4	-0.63	-0.43	-5.1	-3.2	
MOS_Conti_NoRe	-67.3	-310.5	718.1	1392	269.9	2008	100	100	-142.9	-659.2	171.8	964.3	-29.8	-305.0	-0.38	-3.27	-9.5	-15.1	
MOS_Stop_NoRe	-67.3	-54.34	718.1	1392	269.9	269.9	100	100	-142.9	-115.4	171.8	145.0	-29.8	-29.6	-0.38	-0.40	-9.5	-2.9	

340 In the model MOS thus gradually reduces atmospheric CO₂, and thereby also limits global warming with respect to pre-industrial period (Δ SAT, Fig.4); i.e., the temperature increase of 2.14°C by the year 2100 is 0.38 °C lower than Δ SAT of Control_RCP4.5, but still missing the 2°C target.

When AU is deployed in conjunction with MOS the CDR capacity and mitigation effects of MOS are enhanced (Figs.4a&c, Fig.5). By the end of year 2100, 446.8 Pg carbon is sequestered by MOS_AU, an increase of 39.5% relative to normal MOS.
 345 Correspondingly, MOS_AU successfully achieves the 2°C target of the Paris Agreement by maintaining a Δ SAT at 1.89°C relative to pre-industrial (Fig.4c & Tab. 5). As in the run without AU, essentially all of the carbon captured via MOS is stored in the ocean until the end of the 21st century (FR, Tab. 5).

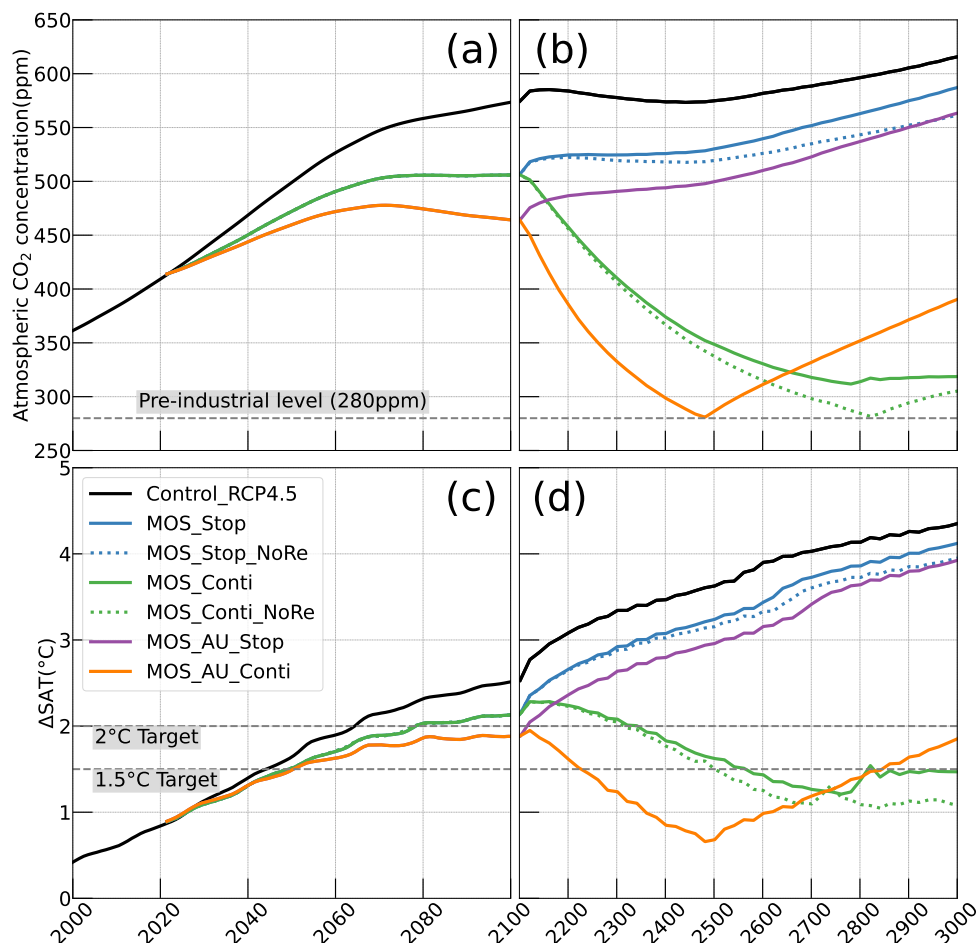


Figure 4. Simulations of: **a, b:** annual global mean atmospheric CO₂ concentration; **c, d:** surface averaged temperature relative to the pre-industrial (averaged of year 1850 to year 1900) level of 13.18°C (Δ SAT). Under RCP4.5 scenario, MOS reaches the 2°C target in conjunction with AU, while the 1.5°C cannot be met in all MOS simulations. Note that MOS is terminated whenever pre-industrial concentrations of atmospheric CO₂ are reached, as seen for MOS_AU_Conti (orange solid) and MOS_Conti_NoRe (blue dotted) in (b&d). Both atmospheric CO₂ and Δ SAT remain lower than control after MOS termination.

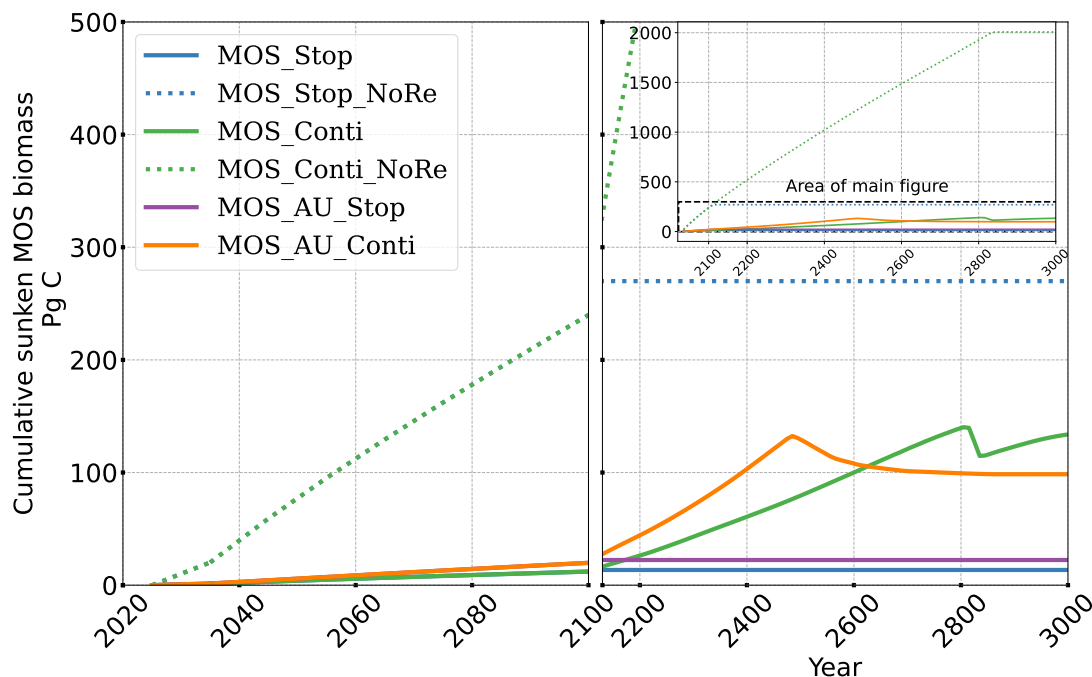


Figure 5. Temporal evolution of globally integrated sunk macroalgal biomass on the sea floor. Biomass generally increases with fertilization by AU. In the idealized zero-remineralization simulations, all sunk macroalgal biomass remains on the seafloor, and globally integrated sunk macroalgal biomass shows a monotonous increase.

4.3.2 Global carbon cycle impacts

The net effect of the MOS-induced climate-carbon cycle perturbation is an increase of the oceanic carbon reservoir (C_{oc}) and a decrease of the atmospheric and terrestrial carbon reservoirs (C_{atm} , C_{ter}). MOS enhances oceanic carbon uptake by increasing the atmosphere to ocean carbon flux (Fig.B10), which is driven by the DIC removal by MOS in the oceans' surface layer. However, the terrestrial carbon reservoir declines (relative to Control_RCP4.5) in all MOS simulations (Tab.5). The atmosphere to land carbon flux is reduced in MOS simulations (Fig.B9). One cause is the photosynthesis reduced by lower CO_2 fertilization of land biota (Keller et al., 2018). This result is in line with other studies showing that CDR can lead to a weakening and even reversal of natural carbon sinks Keller et al. (2018). Besides, it is also worth noting that the increment of C_{oc} in MOS/MOS_AU is 98.2 PgC/163.9 PgC less than the cumulative amount of carbon sunk out of the surface layer via MOS by year 2100 (Tab.5). One reason is that the reduced oceanic carbon uptake by declined PNPP (Sect. 4.3.4) offsets ~37% of the MOS-induced carbon sequestration.

MOS also impacts the distribution of DIC in the ocean. The DIC profiles in Fig.6 illustrate that the general effect of MOS is to move more DIC to greater depth ($z \geq 3000m$). By the end of year 2100, MOS simulations show an increased total DIC concentration in the deeper oceans when compared to Control_RCP4.5 (except for the zero-remineralization sensitivity runs discussed below). For instance, in the deep Southern Ocean, the DIC concentration is on average nearly 80 $\mu mol/kg$ higher



365 than the Control_RCP4.5 in year 2100 (Fig.6). The conjunction of MOS with AU increases average deep ocean DIC even more. An example is the simulated increase of DIC in the deep Pacific Ocean and Atlantic Ocean basins by MOS_AU in year 2100 (orange line in Fig.6 DIC panel). In contrast, DIC concentrations are reduced in shallower waters (depth <1000m) as the air-sea carbon flux is unable to fully compensate the carbon removal by MOS.

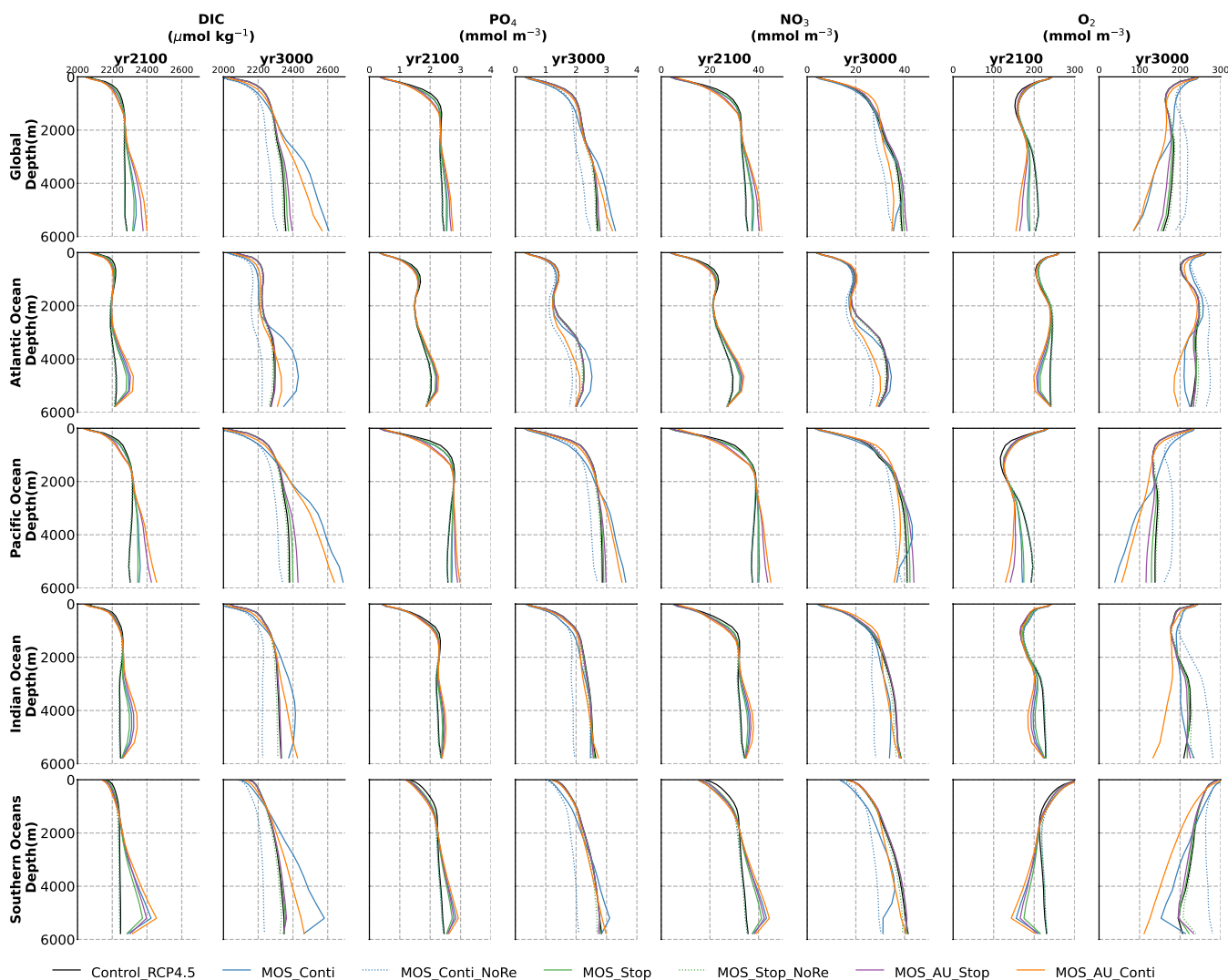


Figure 6. Global and basin-wide averaged vertical profiles of various model tracers in year 2100 and year 3000 under the RCP4.5 emission scenario. In general, MOS (except for the zero remineralization ones) transports DIC and nutrients in the surface layer to the deep ocean. The oxygen levels are increased in the mid layers due to the declined downward organic particle flux (Sect.4.3.4) but decreased in the deep ocean caused by the remineralization of sunk biomass. These impacts are strengthened when MOS is deployed continuously and/or in conjunction with AU.



4.3.3 Impacts on global nutrients distributions

By the year 2100, the deployment of MOS has changed the global patterns of NO_3 and PO_4 . At the surface NO_3 and PO_4 concentrations decrease due to MOS nutrient consumption. In the deep ocean (depth $\geq 3000\text{m}$), PO_4 and NO_3 increase due to the remineralization of sunk macroalgal biomass (except for the MOS_NoRe simulations). The largest increase in deep ocean PO_4 appears in the Southern Ocean, while the smallest increase is found in the Indian Ocean (PO_4 yr2100 groups in Fig.6). This is caused by the distribution of MOS in the surface layer, which in our simulations occupies large areas in the Southern Ocean but only a relatively small region in the Indian Ocean (Fig.2.1).

The remineralization of sunk biomass consumes dissolved oxygen and releases NO_3 and PO_4 . As can be seen from the NO_3 -yr2100 and O_2 -yr2100 panels of Fig.6, deep ocean nutrients generally increased when O_2 is diminished (Sect.4.3.5), as expected from aerobic respiration of sunk biomass. Low-oxygen environments and the associated switch from aerobic remineralization to denitrification, however, occupy relatively small areas, so that this impact is not easily detectable in global nutrient profiles.

4.3.4 Impacts on simulated pelagic ecosystems and the organic particle export

In our simulations, large scale deployment of MOS has an impact on pelagic ecosystems, mainly on phytoplankton NPP (PNPP) and on biomass.

In the MOS simulation, the globally integrated annual PNPP decreases by 20% (9.5 PgC/yr) by year 2100 (Tab. 5). One reason is the canopy shading effect of the floating macroalgae farms, which reduces downward solar radiation available for the phytoplankton community below. In addition, there is nutrient competition between macroalgae and phytoplankton. As shown in Fig.7a, by the end of the 21st century, PNPP declines in MOS areas, e.g. northern and eastern equatorial Pacific and the Southern Ocean. Intriguingly, in a few regions outside the MOS deployment region, PNPP increases instead. For instance, a 'halo' of enhanced PNPP can be observed surrounding the eastern equatorial Pacific MOS region (Fig.7.a). Similar circumstances are simulated in the North Pacific, the Southern Ocean (60°E : 120°E , 30°S) and off the equatorial west coast of Africa. This PNPP-enhancement is sustained by the outflow of residual NO_3 from MOS deployment regions (see Fig.B8). One reason is that the P:N ratio in macroalgae model (1:10) is higher than the Redfield ratio (1:16) in the UVic ESCM, leading to a relatively smaller NO_3 demand by macroalgae growth and some relaxation of nitrogen limitation in phytoplankton. Besides, as described in Sect.2.2.1, the macroalgae growth is constrained by the maximum biomass yield. Thus, macroalgae nutrient uptake cannot compensate the loss of nutrient consumption by light-limited PNPP, especially when AU supplies additional nutrients to the surface.

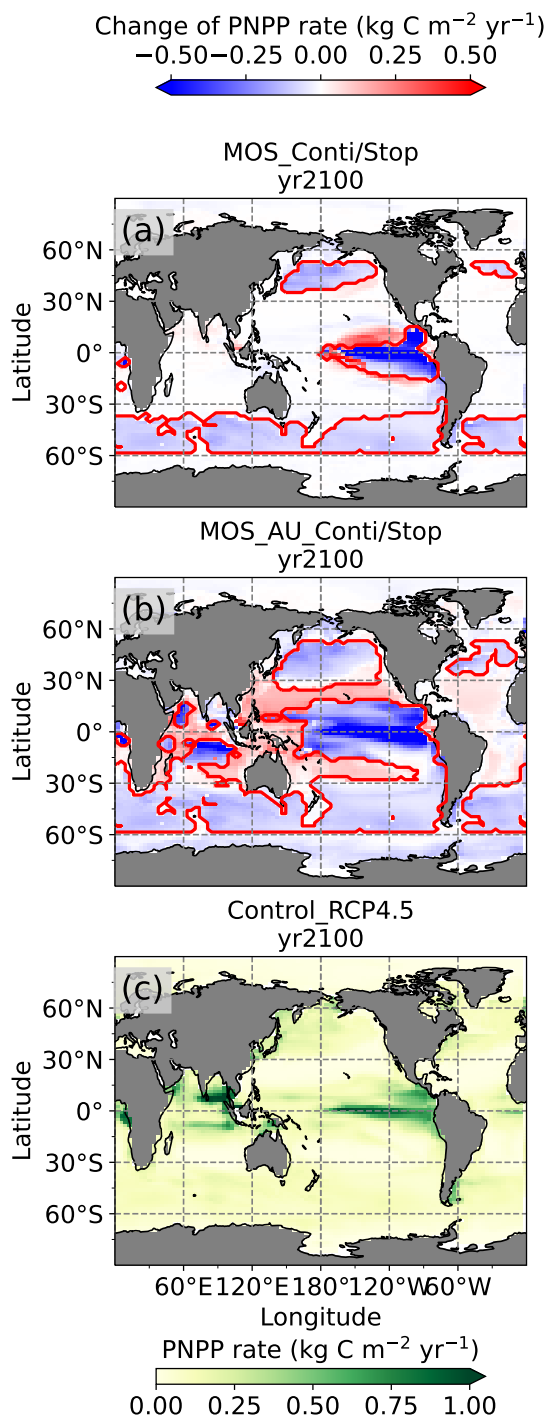


Figure 7. Vertically integrated annual PNPP in year 2100. **a&b:** MOS minus Control_RCP4.5 with red boundaries contouring the MOS occupied area; **c:** Control_RCP4.5. **a** illustrates a decline in PNPP in MOS occupied areas accompanied by a 'halo' of enhanced PNPP surrounding MOS areas, particularly in the ETP caused by the leakage of residual nutrients (Sect.4.3.4). These impacts on PNPP are amplified in MOS-AU (**b**).



In the MOS_AU simulations, the PNPP 'halo' can be seen in almost the whole MOS-free ocean surface (Fig.7.b). The AU
395 fertilization effect enhances the nutrient leakage from the MOS area. This leads to a higher PNPP in MOS_AU than in the
normal MOS simulations (Fig.7.c), but still lower than in the Control_RCP4.5 run (Fig.8.a1).

Changes in the global particle organic carbon (POC) export flux generally follow the pattern of PNPP changes (Fig.8.b1).
Thus, when MOS is present, the PNPP reduction results in a weakened POC flux.

As the zooplankton grazing preference for macroalgae is lower than for phytoplankton the zooplankton community is still
400 mainly fed by phytoplankton. Therefore, the declines in zooplankton biomass (Fig.B3) agree with the declining phytoplankton
biomass trend (Fig.B5).

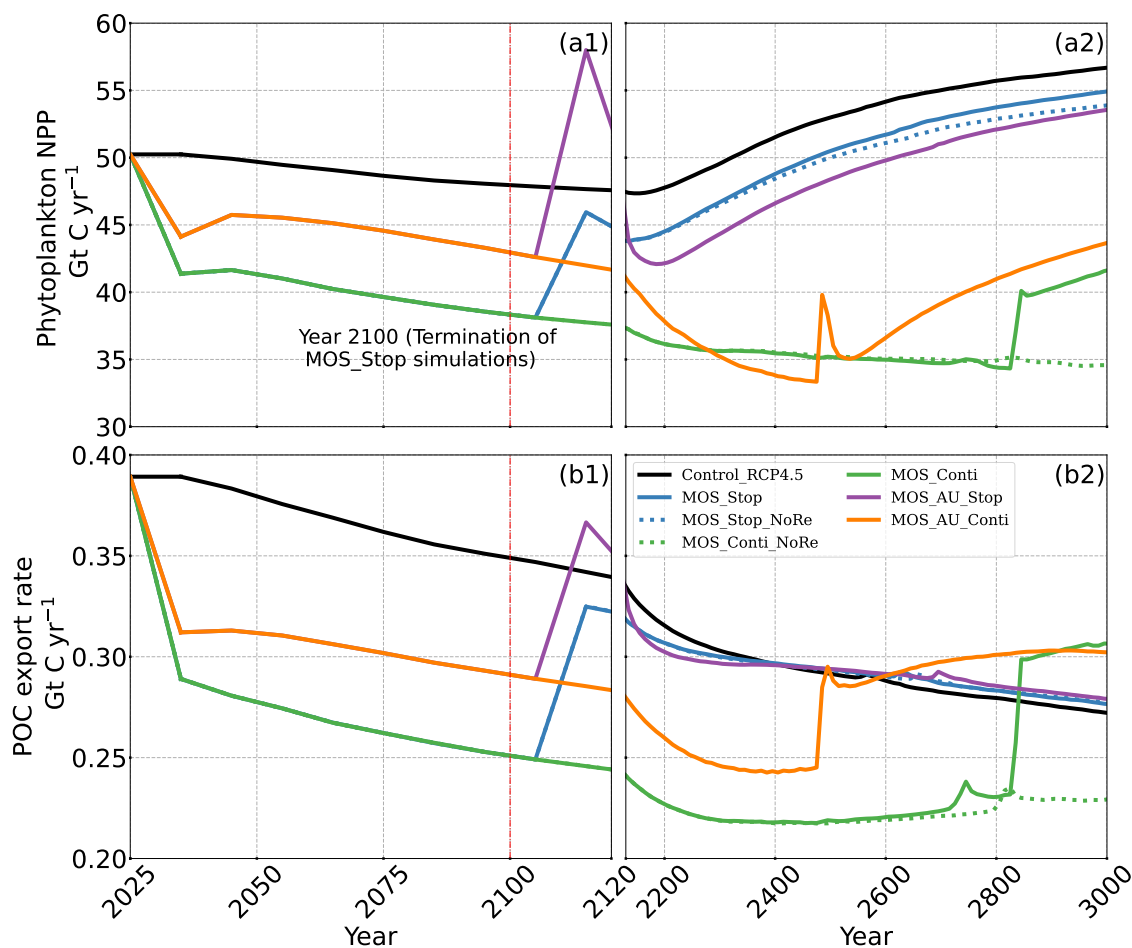


Figure 8. Temporal evolution of globally integrated PNPP (a1, a2); downward POC flux at 2km depth (b1, b2). The termination runs branch off of the continuous ones in year 2100 and are identical up to that point. Through the 21st century, MOS reduces PNPP and POC export due to canopy shading and competition for nutrients. Obvious rebounds followed by quick decline can be observed right after terminations of MOS.



4.3.5 Impacts on dissolved oxygen

The two major impacts of MOS on oceanic dissolved oxygen are: 1) increased deoxygenation at the sea floor by the remineralization of sunk macroalgal biomass (except for MOS_NoRe) and 2) increased dissolved oxygen at mid depths (e.g. 405 300m depth) caused by the reduction of the downward POC flux and the associated decline in oxygen consumption by POC remineralization.

In Control_RCP4.5, the global oceanic dissolved oxygen inventory decreases throughout the simulation. The two main driving mechanisms are the reduced solubility in the warming ocean and the decelerating overturning circulation. The long-term decline of oxygen is especially obvious at depth (1200m), which is induced by increasing deep water residence times and 410 the accumulation of respiratory oxygen deficit under global warming (Oschlies et al., 2019; Oschlies, 2021).

As a result of reduced respiration in the upper water column, the size of the oxygen minimum zone (OMZ) in Eastern Tropical Pacific (ETP) shrinks substantially, and the volume of waters with $O_2 < 80 \text{ mmol/m}^3$ in the North Pacific even disappears. In the Southern Ocean dissolved oxygen increases as well (Fig.9.c). This is more pronounced when AU is applied (Fig.9.e). The increase in dissolved oxygen is caused by decreased microbial remineralization of POC, a consequence of the 415 reduced downward POC flux resulting from the inhibition of PNPP in the surface layer (Sect. 4.3.4). Some decrease in oxygen concentrations occurs in the western Pacific and the Indian Ocean (Fig.9.g), where the surface PNPP is enhanced by the surplus nutrients leaked out from MOS occupied area (see Sect.4.3.4 and Fig.7.c).

Fig.9.d&f and the O_2 yr2100 panel of Fig.6 illustrate how MOS changes the dissolved oxygen in the deeper ocean. Within the normal MOS simulations, the decline of benthic dissolved oxygen mainly happens in the Southern Ocean by year 2100 420 with the appearance of a few new areas with oxygen concentrations less than 80 mmol m^{-3} (Fig.9.d). However, when AU is also deployed, the increased macroalgal biomass sinking and remineralization creates even more benthic OMZs (Fig.9.f) in the benthic ETP and North Pacific Ocean. These new benthic OMZ locations correspond to MOS-occupied surface areas.

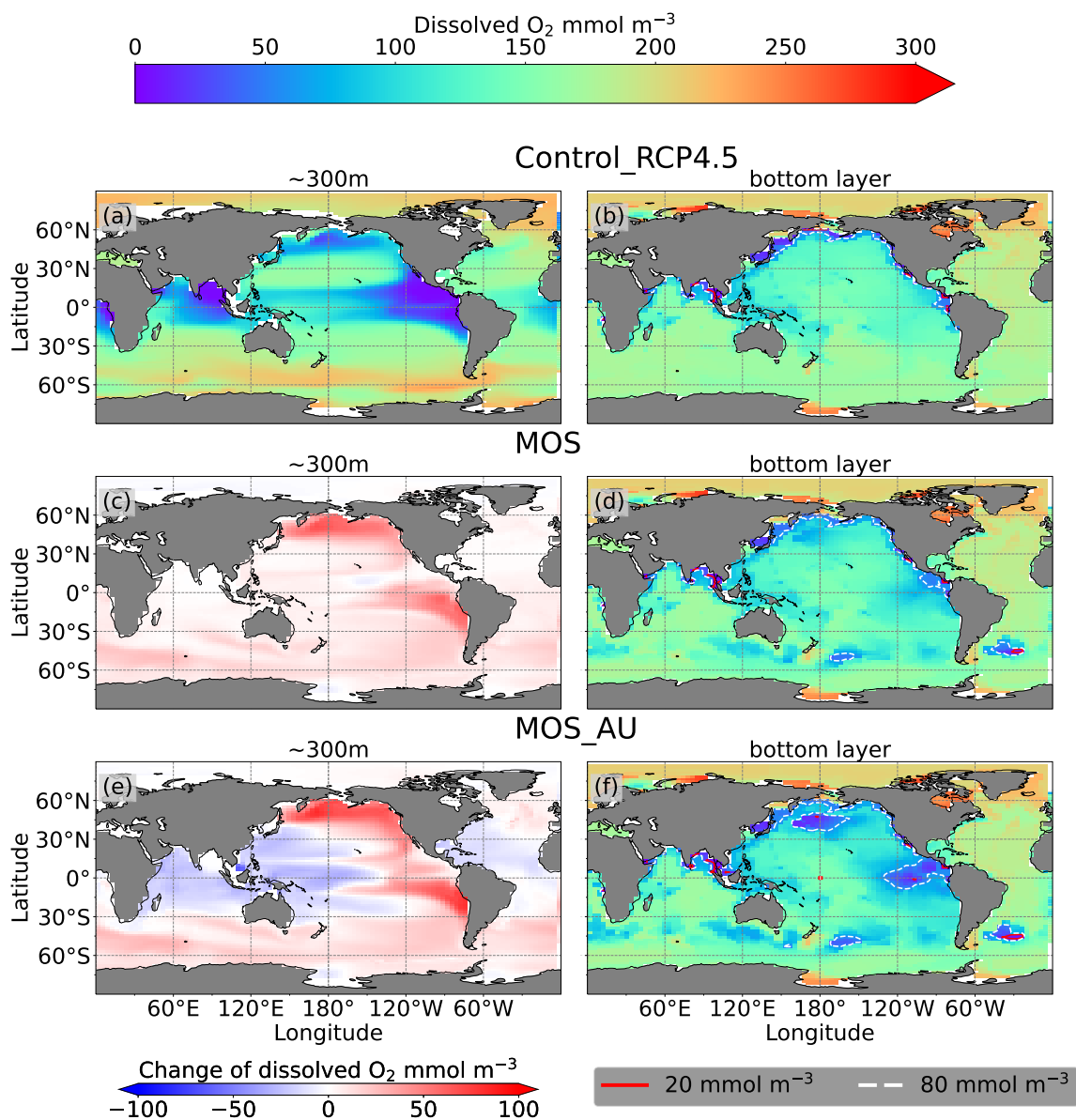


Figure 9. Dissolved O₂ concentration distribution in year 2100 at 300m depth (a, c, e) and the seafloor (b, d, f); lines delineate boundaries of OMZs anywhere within the water column with less than 80 mmol m⁻³ oxygen (white dashed) and less than 20 mmol m⁻³ (red solid). At 300m depth, dissolved oxygen levels are raised in MOS simulations caused by the decline in POC export (c), exception are the reduced oxygen concentrations in regions outside the MOS-AU deployment (e). On the seafloor, remineralization of sunk biomass and creates several new low-oxygen areas (d, f).



4.4 Long-term effects of MOS

Here we will analyse the long-term effects of hypothetical massive MOS deployment beyond the Paris Agreement time frame
425 on a millennial timescale.

Even after a simulated continuous millennial-scale deployment, the distribution of MOS in year 3000 is nearly identical to
the one in year 2100 with only a minimal decrease in biomass (Fig.B1.b). When deployed beyond the year 2100 (MOS_Conti),
MOS will continue to sequester carbon and reduce atmospheric CO₂ on millennial timescales or, in our set-up, until atmospheric
CO₂ falls back to the pre-industrial level of 280ppm. The MOS_Conti simulation ultimately sequesters 2533 PgC and decreases
430 atmospheric CO₂ to 318.5ppm CO₂ by the year 3000, but never achieves the pre-industrial CO₂ level. Notably, atmospheric
CO₂ stops decreasing by year 2780 and rebounds afterwards even though MOS continues to sequester carbon. This can be
explained by a recurrent deep convection in the Southern Ocean around year 2800 that accelerates oceanic carbon leakage
back to the atmosphere (Martin et al., 2013; Reith et al., 2016; Oschlies, 2021). Meanwhile, the leakage of MOS-captured
carbon eventually offsets the MOS carbon sequestration (Sect.4.6).

435 In the sensitivity simulations MOS_Conti_NoRe and MOS_AU_Conti, atmospheric CO₂ reaches 280ppm by the year 2820
and 2475, respectively. After reaching 280ppm, MOS is stopped and atmospheric CO₂ increases again as remineralized car-
bon leaks out of the ocean and the surface ocean adjusts to the no MOS situation. The largest increase in CO₂ is found in
MOS_AU_Conti. Meanwhile, when MOS is deployed (uninterruptedly or till the CO₂ 280ppm trigger), the land carbon up-
take is constantly lower than the control level owing to the reduced CO₂ fertilization effect. Due to the permanent storage of
440 MOS-C in sunk biomass, rebounds of atmospheric CO₂ are relatively gentle in MOS_Conti_NoRe (Fig.B10). Nevertheless,
the atmospheric CO₂ levels in continuous MOS simulations are significantly lower (35% to 50% of Control_RCP4.5) by the
end of year 3000.

The side effects of MOS also persist and often grow in magnitude with continuous deployment. Though PNPP is enhanced
around MOS areas by nutrient leakage (PNPP 'halo', see Sect.4.3.4), the global reduction of surface nutrients and local
445 canopy shading by MOS leads to continuous but gentle lowering of global PNPP after the sharp decreases in the initial 20
years (Fig.8.a2). For instance, in MOS_Conti, PNPP drops by ~60% by the end of year 3000 (Tab. 5). Correspondingly, in
MOS_Conti POC export eventually declines by 50% relative to Control_RCP4.5 (Fig.8b2). In sensitivity run MOS_AU_Conti,
the nutrient supply by AU, which initially maintains a higher phytoplankton biomass and NPP than in MOS without AU
(Sect.4.3), declines with time as source waters of the upwelling become reduced in nutrients. Therefore, PNPP as well as the
450 POC export levels drop after year 2200 (Fig.8.a2&b2).

The redistribution of DIC and nutrients is intensified in the continuous simulations. As shown in Fig.6, when remineralization
of MOS sunk biomass is turned on, the Pacific deep ocean and the Southern deep ocean show the highest DIC and PO₄
enrichment by year 3000. The accumulations depend on ocean circulation (e.g., thermohaline circulation) and the distribution
of MOS at the surface. In MOS_Conti_NoRe, the ocean DIC decreases globally relative to Control_RCP4.5. This results from
455 the continuous DIC removal into biomass via MOS with no remineralization. Another cause of the declined global DIC is the



declining downward POC flux owing to the PNPP reduction caused by the declining nutrient levels in the surface layer (see Sect.4.3.4).

NO₃ enrichment in the deep ocean is considerably smaller than that of DIC and PO₄, because of enhanced denitrification in the developing benthic OMZs (Sect.4.3.5, Fig.B2). In the zero remineralization situations, deep ocean PO₄ and NO₃ concentrations decrease compared to the control levels, due to the reduced remineralization of POM resulting from the weakened downward flux of POM.

As shown in Fig.10 and the O₂ yr3000 panel of Fig.6, dissolved oxygen concentrations at mid depth (e.g. 300m) increased during millennial MOS deployment due to reduced PNPP and associated downward flux and remineralization of POM in the water column. In benthic waters, regions with very low dissolved oxygen are shown in Fig.10.f&j in the Pacific and Southern Ocean. In contrast, increased oxygen concentrations are found in MOS_Conti_NoRe (Fig.10.h), especially in the Atlantic, the Indian and the Southern Ocean. Besides the absence of oxygen consumption by macroalgal biomass remineralization, another reason for these observable oxygen increases lies in the reduction of POC downward flux described in Sect. 4.3.4.

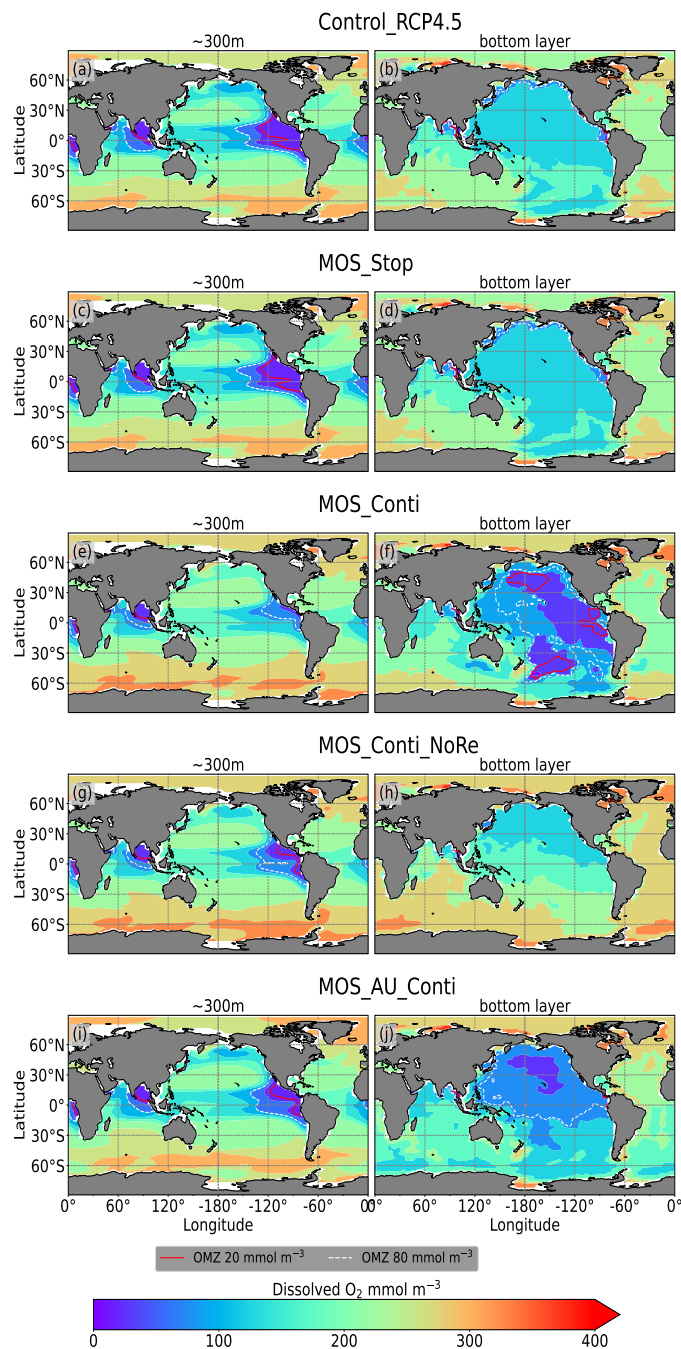


Figure 10. Dissolved O_2 concentrations at depth $\sim 300\text{m}$ (left panel) and the ocean bottom (right panel) in year 3000: contour lines indicate boundaries of OMZs with less than 80 mmol m^{-3} oxygen (white dashed) and less than 20 mmol m^{-3} (red solid). Continuous MOS deployment further shrinks the OMZ at 300m depth (e,g,i) but expands them at bottom (f,j) except for the zero remineralization one in (h).



4.5 Termination effects

After termination of MOS_Stop in year 2100, the atmospheric CO₂ concentrations and SAT both rise, but generally remain
470 lower than those of the Control_RCP4.5 simulation (Fig.4.b,d). More than half (**FR** ranges from 58.6% to 64.4%, Tab.5,
calculated by Eq. 23) of MOS-captured carbon is still stored in the ocean by the end of year 3000. As shown in Fig.4.b,d,
in the termination simulations MOS_Stop and MOS_AU_Stop CO₂ concentration and SAT gradually converge against the
Control_RCP4.5 run as a result of DIC from remineralized macroalgal biomass being transported to the ocean surface and
into the atmosphere (see subsequent Sect.4.6). By year 3000, the atmospheric CO₂ in MOS_Stop is only 28.5 PgC less than
475 in Control_RCP4.5, while ΔSAT slightly rebounds from -0.38°C to -0.23°C. In MOS_AU_Stop, the differences of pCO₂
and ΔSAT are smaller than the normal MOS, as AU has augmented MOS carbon sequestration and 64.4% of it is retain
in the ocean. As expected, the idealized non-remineralization condition (MOS_Stop_NoRe) is able to permanently store the
sequestered carbon, thus the rebounds of CO₂ and ΔSAT are less than the normal MOS_Stop.

In all MOS termination simulations, PNPP and POC export rebound abruptly following the cessation of MOS, but sharply
480 drop over the subsequent decades (Fig.7.a1). The sharp increase in PNPP and POC export results from the sudden absence
of macroalgae as a main competitor for nutrients and light. The subsequent decline in PNPP and POC export results from
consumption of the surface nutrients and the lack of subsurface nutrients that has previously been exported directly to the
seafloor with sinking of macroalgae biomass (Fig.B6). Afterwards, PNPP recovers gradually due to the slow returning of
remineralized nutrients to the upper ocean. By the year 3000, PNPP in MOS_Stop recovers to 97% of the control level (Tab. 5),
485 with the only differences attributable to the slightly different climate state. In the MOS_NoRe simulation, the PNPP recovery is
slower due to the permanent nutrient removal from the upper water column. In the MOS_AU_Stop simulation PNPP rebounds
to higher levels than the normal MOS, but drops to lower levels afterwards. The amplified oscillation of PNPP results from
the simultaneous termination of AU and MOS: When MOS_AU_Stop is suddenly terminated, the canopy shading and nutrient
competition by MOS are removed. Meanwhile, the surplus of nutrients from AU still remains. This boosts PNPP rapidly.
490 However, once these nutrients are consumed, the natural nutrient supply to surface waters is insufficient to maintain the high
PNPP.

After the termination of MOS, the rate of oceanic carbon uptake falls abruptly (Fig. B10). After a short peak caused by the
abrupt rebound of PNPP, it remains slightly lower than the control level due to the declined PNPP rates and lower atmospheric
CO₂ levels. Oppositely, the MOS-induced reduction in terrestrial carbon uptake starts to rebound after MOS cessation (Fig.B9)
495 due to the rise of atmospheric CO₂, which tend to enhance the terrestrial photosynthesis.

When MOS deployment is stopped, the elevated (compared to Control_RCP4.5) dissolved oxygen concentrations at mid
depth generally decline as the downward POC flux recovers (O₂ yr3000 panel in Fig.6). The lowered oxygen concentrations
in the deep ocean are also reversible after cessation of MOS. For instance, by year 3000, the benthic dissolved oxygen of
MOS_Stop (Fig.9.d) is similar to Control_RCP4.5 (Fig.9.b).



500 4.6 Leakage of MOS Sequestered Carbon

The leakage of MOS sequestered carbon (MOS-C) occurs mostly in the Southern Ocean (Fig.11, Fig.B4). The explanation lies in the dynamics of Southern Ocean upwelling, where Pacific Deep Water (PDW), Indian Deep Water (IDW) and Antarctic Deep Water (AADW), laden with DIC of remineralized MOS biomass, reach the subantarctic ocean surface (Talley, 2013; Weber and Bianchi, 2020; Anderson and Peters, 2016). Moreover, the recurrent deep convection (see Sect.4.4) in the Southern Ocean around year 2600 accelerates the carbon leakage, which can be observed in Fig.11 as an enhanced outgassing around year 2600.

The outgassing of MOS-C in discontinuous simulations (e.g. MOS_Stop) starts since year 2100, while the continuous ones starts since year 2300 (Fig.11). Thus, by the end of the 21st century, nearly the entire MOS-C in all MOS simulations is retained in the ocean. However, by the year 3000, even in the continuous MOS simulation, only about 75% of MOS-C remains in the ocean, while the accelerated vertical water transport by AU slightly reduces this portion to 73%. In run MOS_Stop 59% of MOS-C remains in the the ocean by year 3000, whereas the additional sunk macroalgal biomass in MOS_AU_Stop results in more MOS-C (64%) being retained (Tab.5). When sunk biomass is free from remineralization (NoRE runs), the contained carbon is permanently isolated from the atmosphere and stored in the ocean.

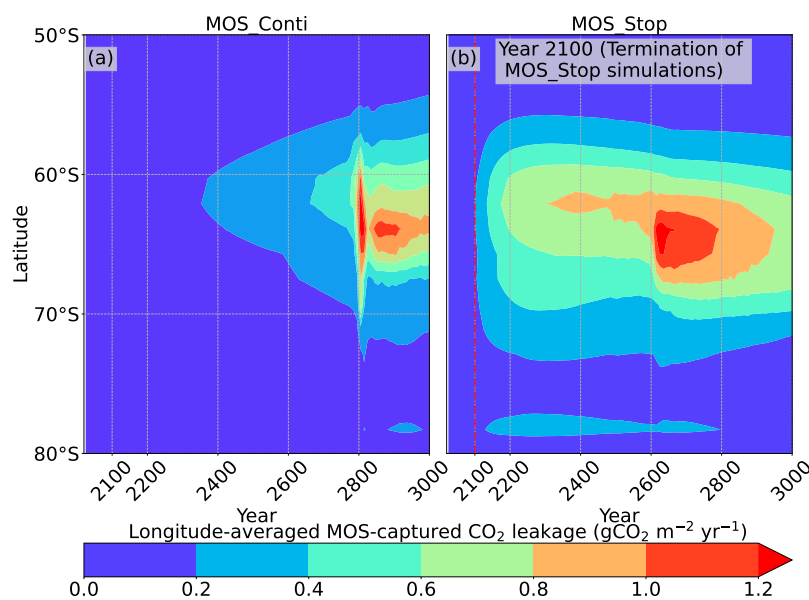


Figure 11. Longitude averaged MOS-captured carbon outgassing in the simulation (a) MOS_Conti and (b) MOS_Stop. When conveyed back to the surface, the DIC from MOS remineralization participates the air-sea exchange (Sect. 2.2.5). MOS-C outgassing starts in year 2100 when MOS is terminated (a), or after year 2300 when continuously deployed. The outgassing mainly happens in the Southern Ocean. The outgassing is strengthened around year 2800 when a Southern Ocean deep convection event accelerates the upwelling of deep waters with high concentrations of remineralized DIC (Sect. 4.4).



5 Concluding discussions

515 In this study we have tested the potential of the ‘macroalgae open-ocean mariculture and sinking (MOS)’ as a carbon dioxide
removal method. Although environmental conditions (e.g. nutrients, temperature, etc.) in the open oceans differ considerably
from the coastal/near-shore regions where macroalgae aquaculture is currently applied in reality, our simulations suggest that
in certain open ocean regions macroalgae may successfully grow and sequester carbon (if engineering constraints can be
overcome). Even for continuous deployment at a maximum scale currently deemed possible, MOS alone is not able to reduce
520 the warming to the 2°C target by the end of the 21st Century under the RCP4.5 moderate mitigation scenario. This finding is
consistent with conclusions from previous studies that no single carbon dioxide removal method alone can ensure reaching the
current climate goals (Keller et al., 2014; Anderson and Peters, 2016; Fuss et al., 2020; IPCC, 2018).

In order to estimate the maximum CO₂ removal potential, the possible synergy of MOS with artificial upwelling (AU) has
been investigated. The employed AU concept aims at piping nutrient-rich deep water to the surface to enhance the growth of
525 macroalgae in MOS. As expected, AU is found to have the potential to successfully enlarge the growing area of MOS and
enhance the CDR capacity of MOS.

In the first 80 years of deployment, the maximum MOS carbon sequestration potential is 3.38 PgC/yr for regular MOS, but
can be boosted up to 5.56 PgC/yr with assistance from AU. If deployment is discontinued from year 2100, about 58.6% to
70.2% (normal MOS and MOS_AU, respectively) of MOS sequestered carbon would be retained in the ocean by year 3000.

530 Several potential side effects have also been revealed and analysed. One side effect is the reduction in phytoplankton NPP
due to canopy shading and nutrient removal from the sea surface to the bottom by MOS. The declined PNPP in turn offsets
~37% of the MOS CDR. Intriguingly, some areas with enhanced PNPP (PNPP ‘halo’, Sect.4.3.4) are found surrounding the
major areas occupied by MOS, fueled by the residual NO₃ that leaks from MOS areas.

Another strong side effect of large-scaled MOS is the impact on oxygen distributions. Dissolved oxygen concentrations
535 increase in near-surface and intermediate waters, as MOS reduces the downward flux of plankton-derived organic matter by
restraining the surface PNPP. On the other hand, the massive amount of sunk biomass from MOS at the ocean bottom and its
subsequent remineralization consumes oxygen and can create large benthic OMZs.

An uncertain factor is the fate of the sunk biomass. It will affect the benthic fauna by depositing large amounts of organic
matter as well as expanding low oxygen regions on the sea floor upon oxygen consumption by remineralization. Therefore,
540 we performed additional sensitivity simulations focusing on the macroalgal biomass remineralization rate. When macroalgal
biomass does not undergo microbial remineralization, the captured CO₂ can be permanently stored without leakage. This in-
creases the CDR potential of MOS. The benthic OMZs created by remineralization of sunk biomass would also be avoided,
while the shrinking of intermediate water OMZs persists. However, other side effects can not be neglected: in zero reminer-
alization simulations, the constant removal of nutrients in the surface will impede the recovery of PNPP. This may eventually
545 affect the marine surface ecology and ocean services such as food provision.

The impacts of MOS on oxygen distributions may also influence the oceanic sources of N₂O, an atmospheric GHG gas and a
major ozone-depleting compound (Ravishankara et al., 2009). The increased/decreased oxygen levels in the mid/bottom layers



impacts denitrification, and may weaken the N_2O sources in the subsurface but increases those in the deep waters (Bange et al., 2019).

550 Moreover, attention should also be paid to the calcification by calcareous macroalgae (if cultivated) and/or associated epibionts that grow on macroalgae. Bach et al. (2021) have suggested that epibionts living on *Sargassum* offsets 16.5% of the POC fixed by *Sargassum* and therefore decrease its natural carbon sequestration potential if the biomass was intentionally sunk for CDR purposes. These calcification rates and the response to ocean acidification of macroalgae are also species-specific Koch et al. (2013). These factors need to be investigated with further research if macroalgae are to be considered for
555 ocean-based CDR, e.g. ocean afforestation (N'Yeurt et al., 2012; Bach et al., 2021).

A side effect not investigated here is the production and emission of halocarbons from macroalgae farms. Macroalgae species have been reported to generate halocarbons in polar, temperate and tropical coastal regions with a highest producing rate of 6000 pmol $CHBr_3$ $gFW^{-1} h^{-1}$ (Leedham et al., 2013; Baker et al., 2001; Carpenter and Liss, 2000; Latumus, 1995). These volatile low molecular-weight halocarbon compounds (e.g. CH_3I , $CHBr_3$ and $CHCl_3$) are potent greenhouse gases (Meinshausen et al., 2011). They also influence stratospheric ozone destruction when transported by deep atmospheric convection
560 into the stratosphere (Ziska et al., 2013; Tegtmeier et al., 2012, 2013), therefore enhancing radiative forcing (Ramaswamy et al., 1992; Daniel et al., 1995). Large-scale MOS cultivation might release a significant quantity of halocarbons. Further studies are needed to investigate possible effects of halocarbon emissions from large-scaled macroalgae cultivation.

Besides the CDR effect of MOS, in case of large scale deployment, the macroalgae farms are likely to increase the albedo
565 of the oceans's surface, especially when they occur near the sea surface (Fogarty et al., 2018; Bach et al., 2021). Meanwhile, we have not considered possible hydrodynamic impacts on ocean circulation, as the thick macroalgae layers and the farming infrastructures may influence the momentum and mixing of the ambient flow fields (Liu and Huguenard, 2020; Nepf, 2012; Thomas and McLelland, 2015).

The MOS model analysis presented here clearly has some limitations, that future studies might improve on. One of the
570 most critical issues is to improve the realism of the model design by including more representative macroalgae species for various regions. Another aspect is the consideration of dynamic cellular stoichiometry of macroalgae. With a better simulation of the cellular quota, we could improve our understanding of the relation of nutrient and carbon fluxes between MOS and the environment. Explicit consideration of the variable morphology of the macroalgae, as well as of the impacts of currents on frond erosion (Broch and Slagstad, 2012) would also improve the representation of macroalgae loss rates in the model. Further
575 optimization of deployment timing and location for MOS are achievable by evaluating data from field tests or implementations of macroalgae mariculture in the open oceans. Another aspect that needs improvement is the modeling of benthic macroalgal biomass remineralization. Here we treated macroalgal biomass homogeneously as particulate organic matter. Though the degradation of macroalgal fragments under deep sea conditions (e.g. low temperature and unique microbial colonies) remains unclear, it might be different from POC in terms of remineralization rate and oxygen consumption. Tracking of macroalgae se-
580 questered carbon will be required to record its fate and possible carbon leakage after sinking (e.g. by an eDNA method to trace macroalgae carbon in marine sediments by D'Auriac et al. (2021)). The economic perspectives of developing and deploying MOS also needs to be investigated. Furthermore, more research on how large-scale macroalgae mariculture will impact human



activities (e.g., ocean shipping, fisheries) needs to be undertaken. Associated legal and political issues regarding the usage of international waters for MOS deployment should be considered as well.

585 Overall, this study adds to the rapidly expanding field of considering macroalgae cultivation for CO₂ removal. The evidence from this study suggests that macroalgae mariculture&sinking has a considerable CDR potential but brings about substantial side effects on marine ecosystems, and marine biogeochemistry. Given this, the concept requires further research with less idealized experimental settings to determine if its CDR benefits outweigh the side effects (Dean et al., 2021).

6 Model codes and data availability

590 The model codes and simulation data are available upon request and will be available online with final publication.

7 Author contribution

J.W., D.P.K. and A.O. conceived and designed the experiments. J.W. implemented and performed the experiments and analyzed the data. J.W. wrote the manuscript with contributions from D.P.K. and A.O.

8 Competing interests

595 The authors declare that they have no conflict of interests.

9 Acknowledgements

D.P.K. and A.O. have been supported by the European Union's Horizon 2020 research and innovation program under grant agreement numbers 869357 (OceanNETs) and 820989 (COMFORT). J.W. has been supported by the China Scholarship Council. We thank Wolfgang Koeve, Nadine Mengis, Karin Kvale and Fabian Reith for helpful discussions.



600 Appendix A: MOS validations

A1 MOS yield calculation

For the convenience of calculation, we assume that when MOS occupies a surface grid cell the area is covered by parallel cultivation ropes (lines) with an interval distance of d (see table 1 & Fig.A1). The total length of cultivation lines (L_{MOS} , in meters) of MOS in the grid cell is then:

$$605 \quad L_{MOS} = S_{MOS} \div d \quad (A1)$$

where $S_{MOS}(\text{m}^{-2})$ is the area of ocean surface occupied by MOS. Accordingly, the conversion between macroalgal biomass yield on ropes (Y_{rope} in kg DW m^{-1}) or in fields (Y_{field} in kg DW m^{-2}) can be calculated as:

$$Y_{rope} = Y_{field} \times d \quad (A2)$$

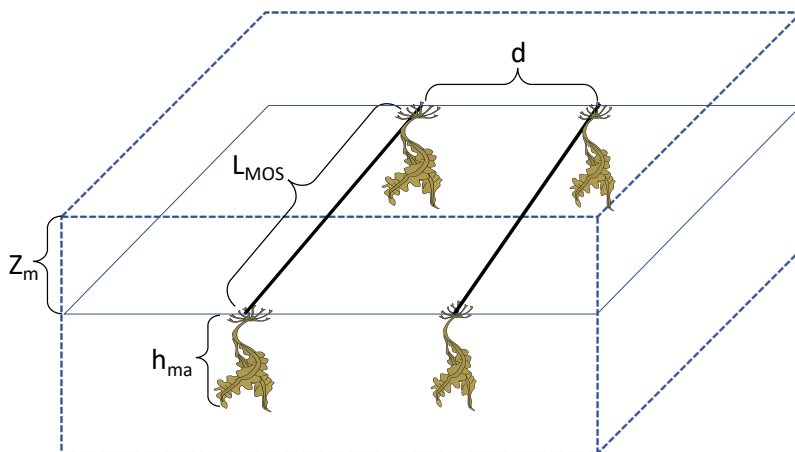


Figure A1. Sketch of key features of MOS.



A2 MOS NPP

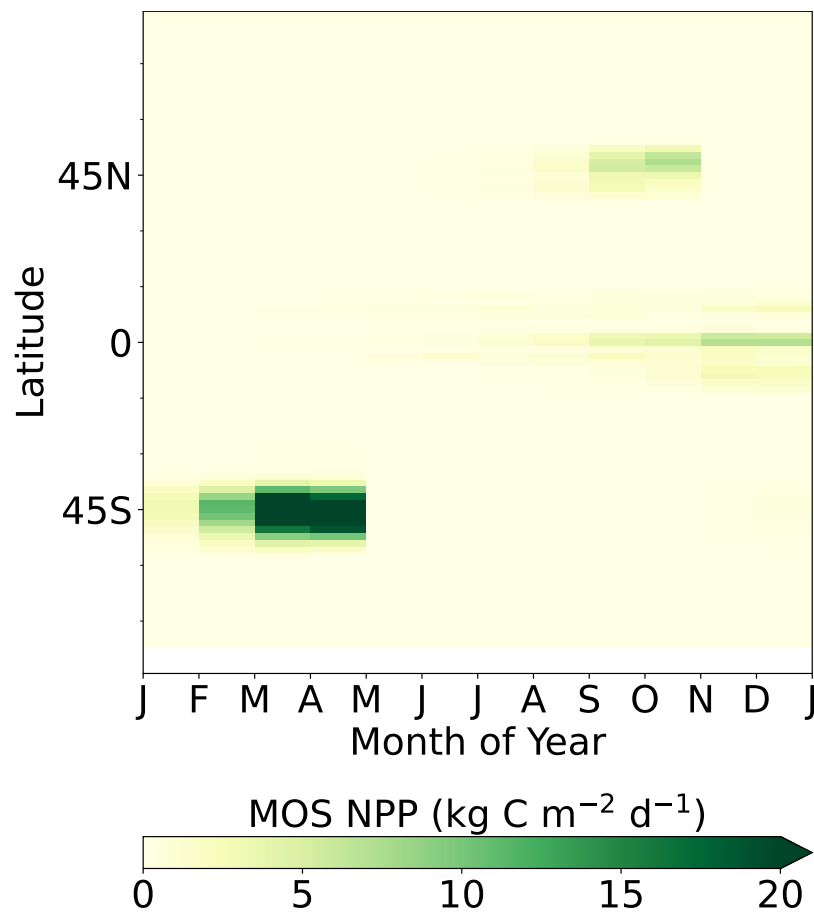


Figure A2. Hovemoeller plot of latitudinally and vertically integrated MOS NPP. High NPP are found in the Southern Ocean. The change of MOS NPP follows the seasonal solar radiation in UVic ESCM.



610 Appendix B: Impacts of MOS on global biogeochemistry

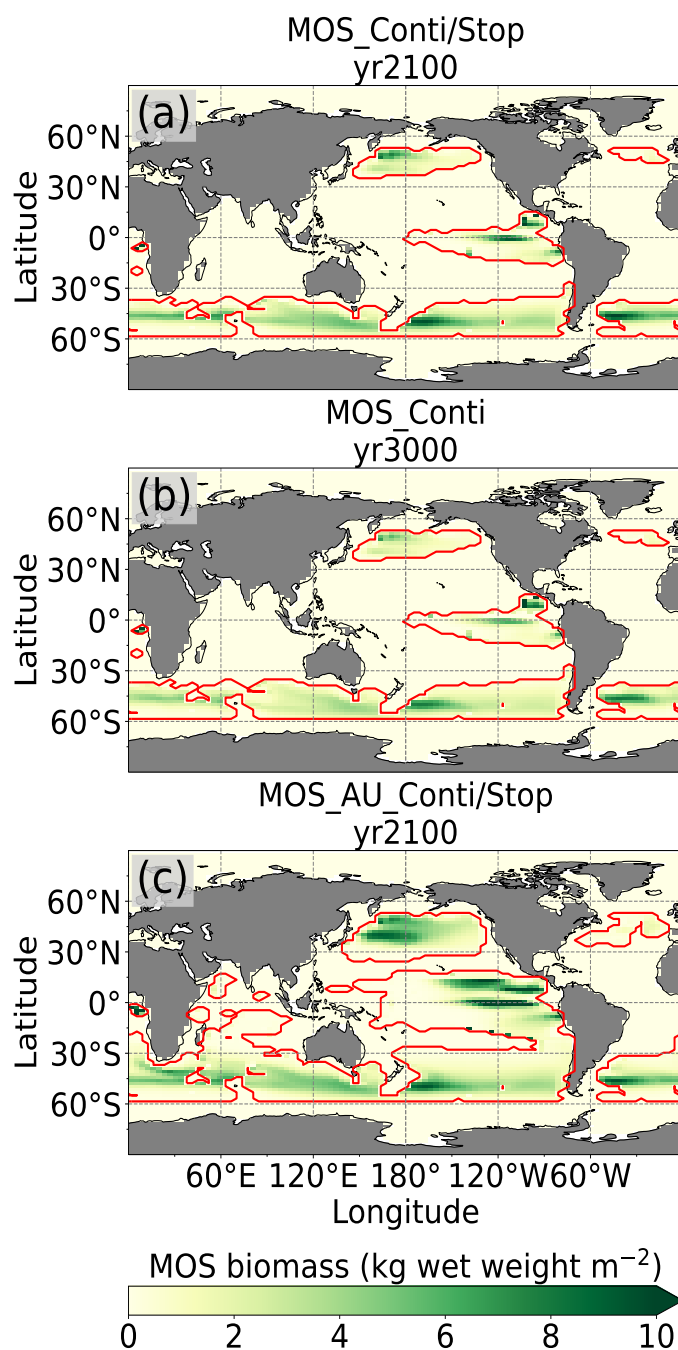


Figure B1. MOS biomass distributions. Red lines contour the maximum MOS occupied area during the previous years.

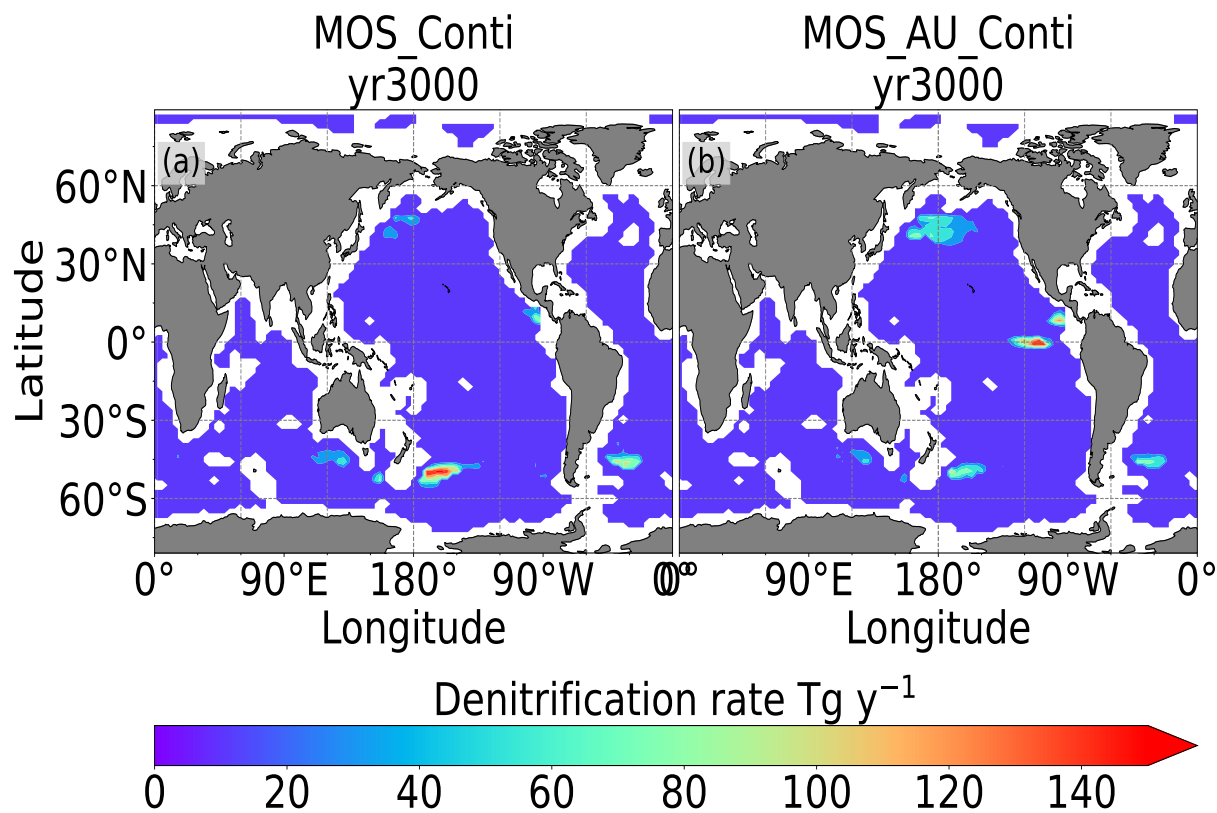


Figure B2. Denitrification rate at depth 3000-6000m in year 3000, where the oxygen level is lower than $5\ \mu\text{mol}\ \text{m}^{-3}$ caused by the remineralization of continuously sunk MOS biomass.

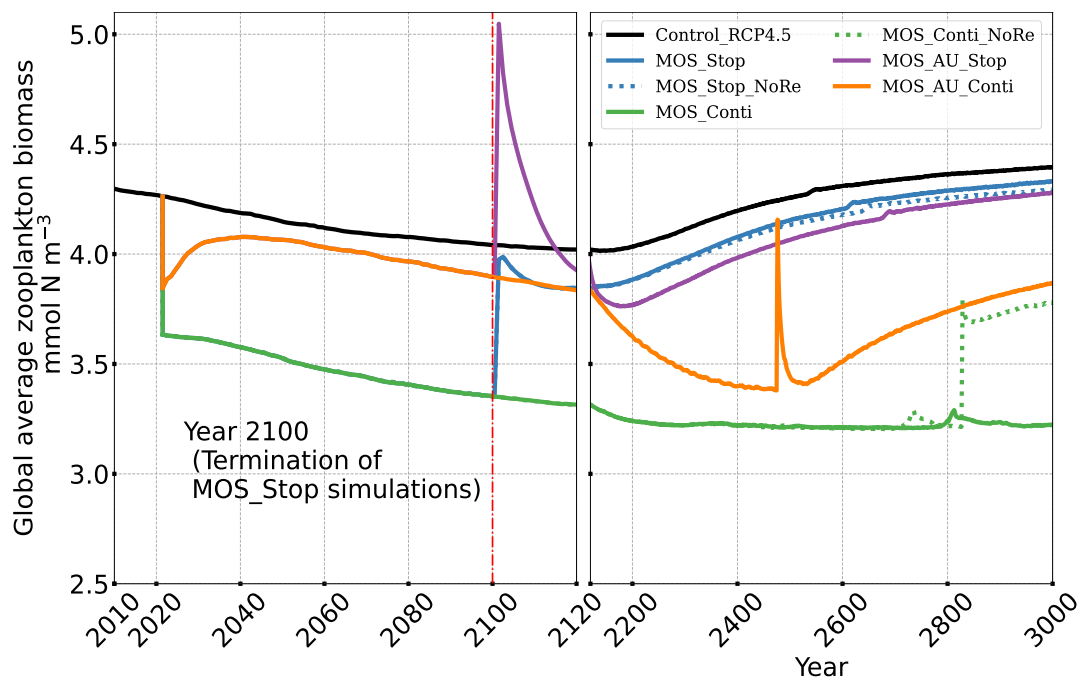


Figure B3. Plot of global averaged biomass of zooplankton

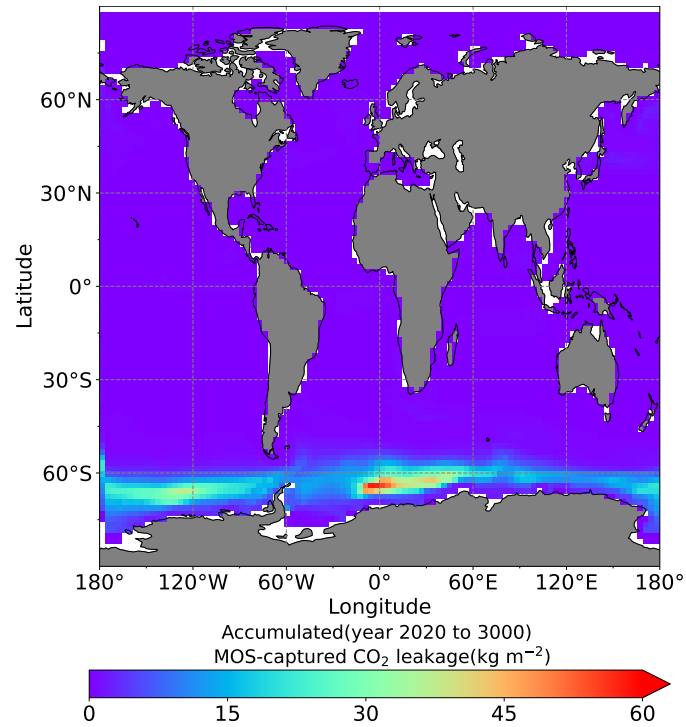


Figure B4. Cumulative (year 2020 to 3000) leakage of MOS-captured carbon in the simulation MOS_Stop.

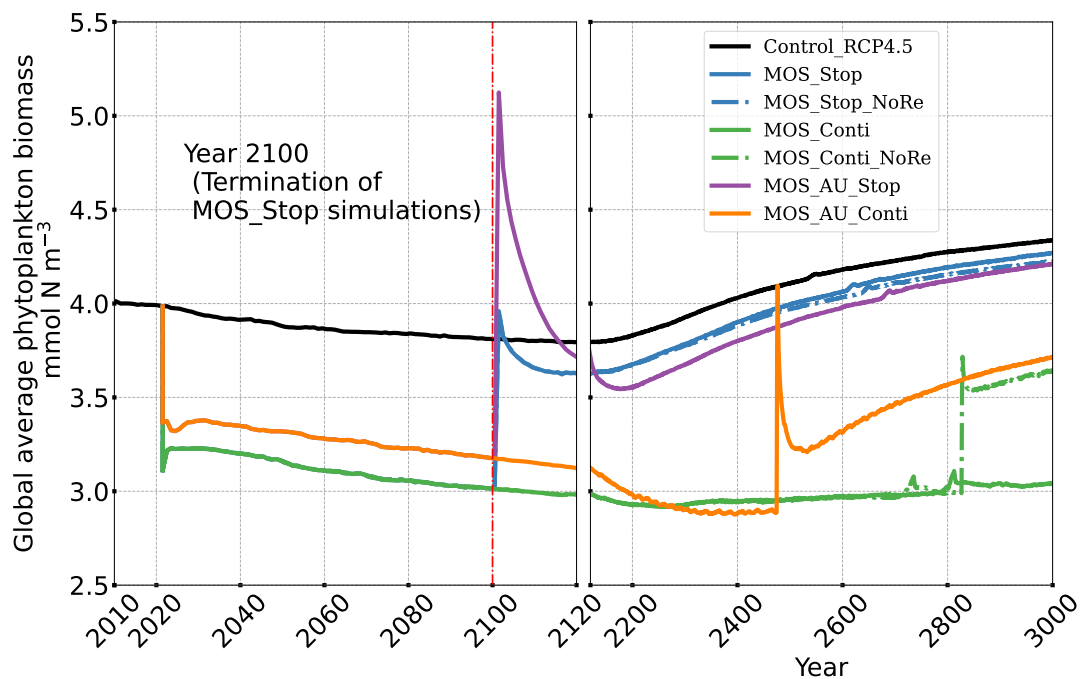


Figure B5. Plot of global averaged phytoplankton biomass

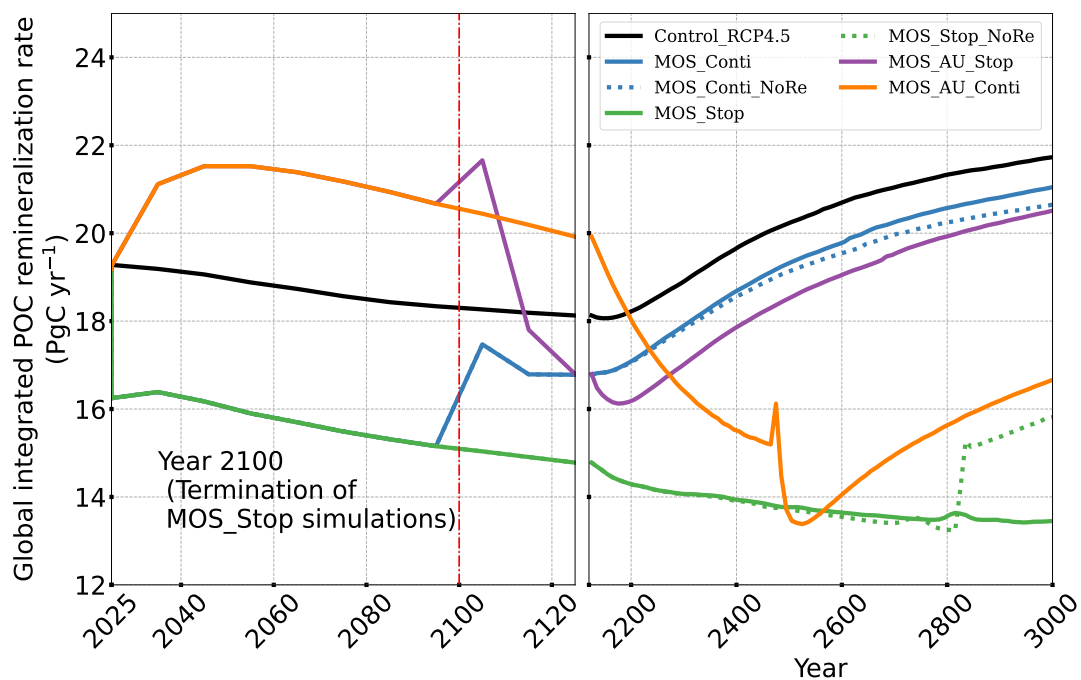


Figure B6. Plot of 0-2km averaged detritus remineralization rate

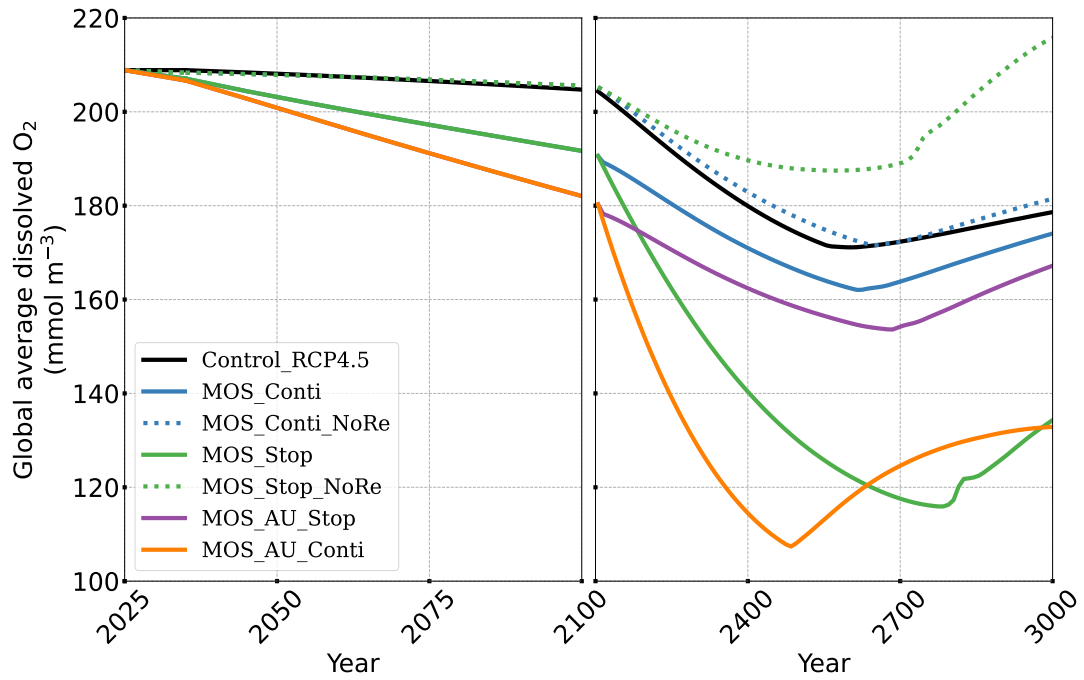


Figure B7. 3-6km averaged dissolved oxygen concentrations

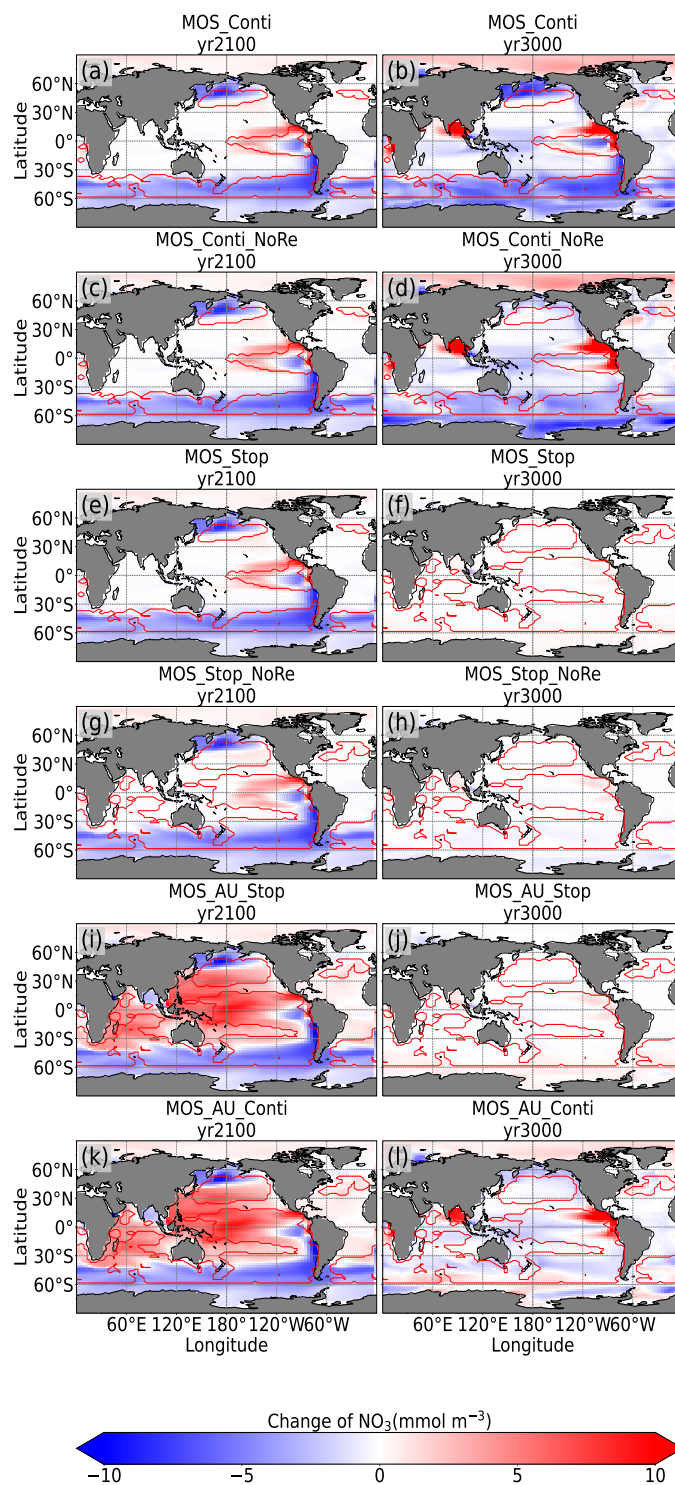


Figure B8. Redistributions of NO_3 avg. 0-200m depth relative to RCP4.5

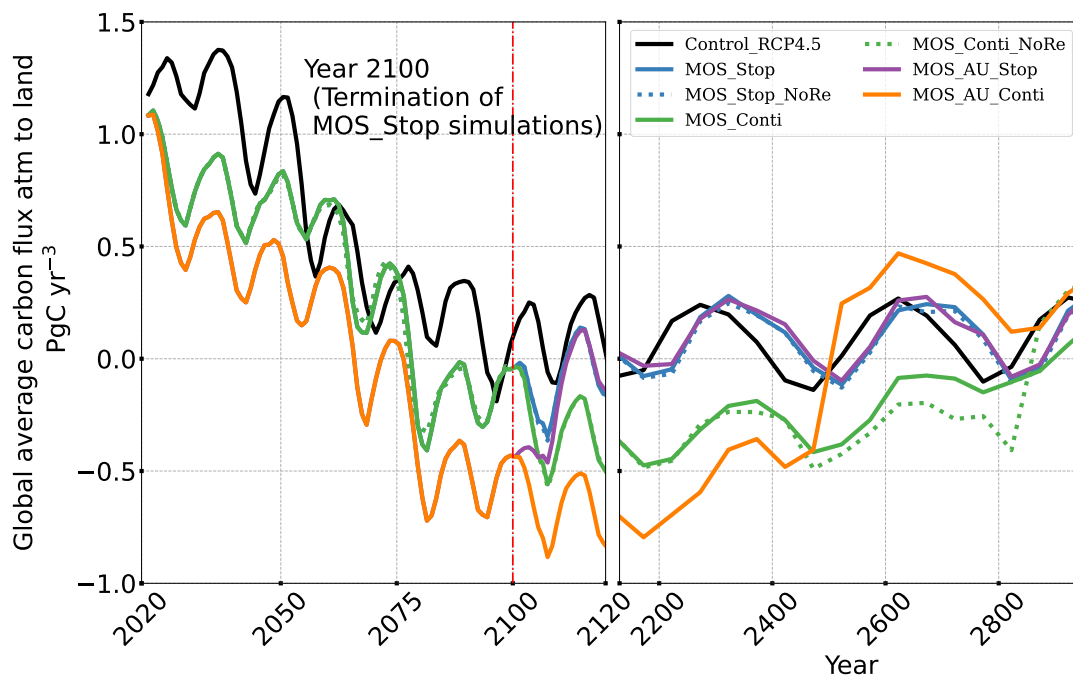


Figure B9. Global averaged carbon flux from atmosphere to land

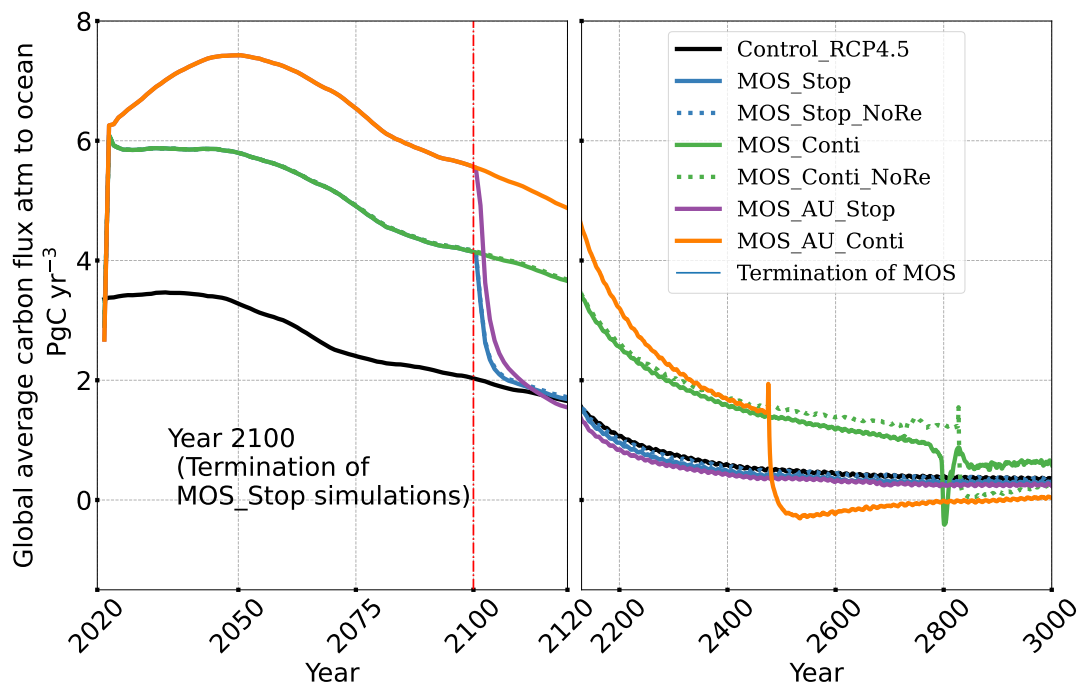


Figure B10. Global averaged carbon flux from atmosphere to ocean



Appendix C: MOS under RCP8.5 scenario

Two MOS simulations are performed under RCP8.5 high emission scenario. To analyse the maximum CDR potential of MOS, macroalgal biomass remineralization rate (u_{max} in Tab.1) is set to zero therein. The sunk macroalgal biomass thus accumulated on the seafloor permanently without interaction with ambient biogeochemistry.

615 Due to the high emissions in RCP8.5, in the beginning 80 years, even the maximum MOS is not able to significantly drop the atmospheric CO_2 concentration ($p\text{CO}_2$) nor the SAT. By the end of 21st Century, 190.3 PgC of C_{atm} is removed from the atmosphere to the oceanic carbon pool. $p\text{CO}_2$ is reduced by 89.7 ppm while SAT descended to 17.48°C with -0.29°C . This mitigation result is far away above the 2°C target, let alone the the 1.5°C ambition (Tab.C1).

620 In MOS_8.5_Conti_NoRe with continuous deployment of MOS, in total 2767 PgC of CO_2 is sequestered by MOS. An obvious reduction of $p\text{CO}_2$ appeared till year 2200, followed by a sharp decrease of 2195 PgC by the end (Tab.C1), resulting in a decreasing of SAT by 2.30°C . Nevertheless, under RCP8.5 scenario with high anthropogenic GHGs emissions, the mitigation capacity of MOS alone is insufficient to counteract the ascent $p\text{CO}_2$ nor global warming relative the results under the RCP4.5 scenario with moderate mitigation.

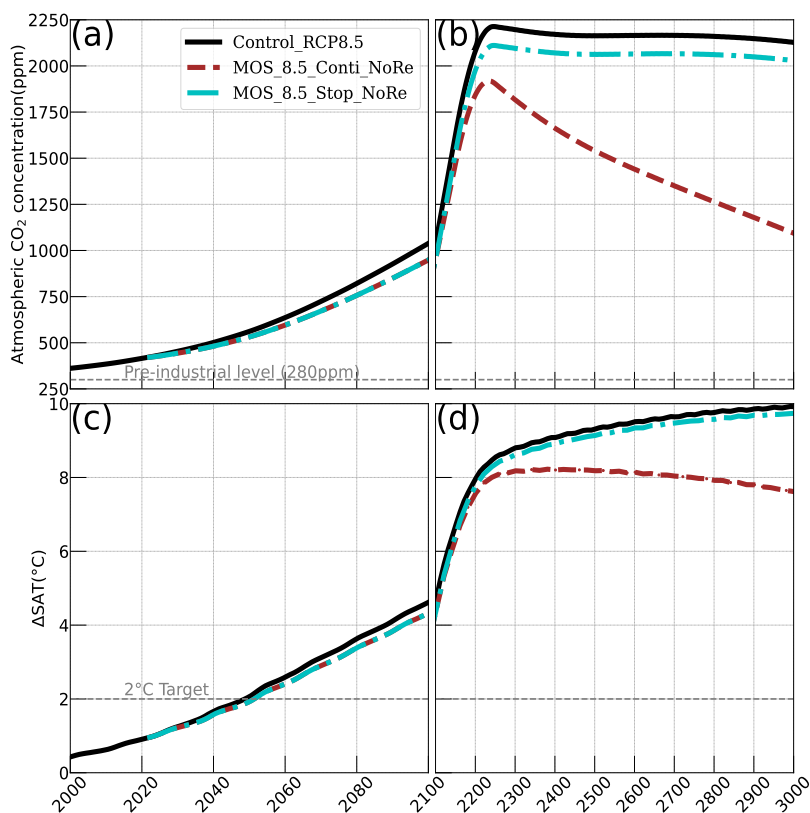


Figure C1. Simulation under RCP8.5 Scenario: a, b: Annual global mean atmospheric CO_2 concentration; c, d: Surface averaged temperature subtracted from pre-industrial level 13.18°C (ΔSAT)



Table C1. Model Simulations under RCP8.5 scenario

Experiment	pCO ₂ (ppm)		Cumulative CO ₂ Emission (PgC)		CDR-MOS (PgC)		Fraction Retained in Ocean (%)		C _{atm} (PgC)		C _{oc} (PgC)		C _{ter} (PgC)		SAT (°C)		Phyt NPP ($\frac{\text{PgC}}{\text{yr}}$)		
	2100	3000	2020-2100	2020-3000	2100	3000	2100	3000	2100	3000	2100	3000	2100	3000	2100	3000	2100	3000	
Control_RCP8.5	1033	2127	2366	5550	/	/	/	/	2193	4517	37765	39369	1832	1706	17.77	23.08	48.57	79.26	
<i>Experiment minus Control_8.5</i>																			
MOS_8.5_Conti_NoRe	-89.7	-1034	2366	5550	260	2767	100	100	-190.3	-2195	196.4	2122	-6.1	72.7	-0.29	-2.30	-8.3	-31.5	
MOS_8.5_Stop_NoRe	-89.7	-98.5	2366	5550	260	/	100	100	-190.3	-209.2	196.4	200.8	-6.1	8.4	-0.29	-0.18	-8.3	-1.2	



References

- 625 Albright, R., Caldeira, L., Hosfelt, J., Kwiatkowski, L., Maclaren, J. K., Mason, B. M., Nebuchina, Y., Ninokawa, A., Pongratz, J., Ricke, K. L., Rivlin, T., Schneider, K., Sesboüé, M., Shamberger, K., Silverman, J., Wolfe, K., Zhu, K., and Caldeira, K.: Reversal of ocean acidification enhances net coral reef calcification, *Nature*, 531, 362–365, <https://doi.org/10.1038/nature17155>, 2016.
- Aldridge, J. N. and Trimmer, M.: Modelling the distribution and growth of 'problem' green seaweed in the Medway estuary, UK, *Hydrobiologia*, 629, 107–122, <https://doi.org/10.1007/s10750-009-9760-6>, 2009.
- 630 Anderson, K. and Peters, G.: The trouble with negative emissions, *Science* (80-.), 354, 182–183, <https://doi.org/10.1126/science.aah4567>, 2016.
- APAR-e, U. D. o. E.: Macroalgae Research Inspiring Novel Energy Resources, <https://arpa-e.energy.gov/technologies/programs/mariner>, 2021.
- Atkinson, M. J. and Smith, S. V.: C:N:P ratios of benthic marine plants, *Limnol. Oceanogr.*, 28, 568–574, <https://doi.org/10.4319/lo.1983.28.3.0568>, 1983.
- 635 Bach, L. T., Tamsitt, V., Gower, J., Hurd, C. L., Raven, J. A., and Boyd, P. W.: Testing the climate intervention potential of ocean afforestation using the Great Atlantic Sargassum Belt, *Nat. Commun.*, 12, 2556, <https://doi.org/10.1038/s41467-021-22837-2>, 2021.
- Baird, M. E., Walker, S. J., Wallace, B. B., Webster, I. T., and Parslow, J. S.: The use of mechanistic descriptions of algal growth and zooplankton grazing in an estuarine eutrophication model, *Estuar. Coast. Shelf Sci.*, 56, 685–695, [https://doi.org/10.1016/S0272-7714\(02\)00219-6](https://doi.org/10.1016/S0272-7714(02)00219-6), 2003.
- 640 Baker, J. M., Sturges, W. T., Sugier, J., Sunnenberg, G., Lovett, A. A., Reeves, C. E., Nightingale, P. D., and Penkett, S. A.: Emissions of CH₃Br, organochlorines, and organoiodines from temperate macroalgae, *Chemosph. - Glob. Chang. Sci.*, 3, 93–106, [https://doi.org/10.1016/S1465-9972\(00\)00021-0](https://doi.org/10.1016/S1465-9972(00)00021-0), 2001.
- Bange, H. W., Arévalo-Martínez, D. L., de la Paz, M., Farías, L., Kaiser, J., Kock, A., Law, C. S., Rees, A. P., Rehder, G., Tortell, P. D., 645 Upstill-Goddard, R. C., and Wilson, S. T.: A harmonized nitrous oxide (N₂O) ocean observation network for the 21st century, *Front. Mar. Sci.*, 6, 1–10, <https://doi.org/10.3389/fmars.2019.00157>, 2019.
- Bird, M. I., Wurster, C. M., de Paula Silva, P. H., Bass, A. M., and de Nys, R.: Algal biochar - production and properties, *Bioresour. Technol.*, 102, 1886–1891, <https://doi.org/10.1016/j.biortech.2010.07.106>, 2011.
- Bitz, C. M. and Lipscomb, W. H.: An energy-conserving thermodynamic model of sea ice, *J. Geophys. Res. Ocean.*, 104, 15 669–15 677, 650 <https://doi.org/10.1029/1999jc900100>, 1999.
- Bowie, G., Mills, W., Porcella, D., Campbell, C., Pagenkopf, J., Rupp, G., Johnson, K., Chan, P., Gherini, S., and Chamberlin, C.: Rates, constants, and kinetics formulations in surface water quality modeling, *Epa*, 600, 3–85, 1985.
- Breeman, A. M.: Relative importance of temperature and other factors in determining geographic boundaries of seaweeds: Experimental and phenological evidence, *Helgoländer Meeresuntersuchungen*, 42, 199–241, <https://doi.org/10.1007/BF02366043>, 1988.
- 655 Broch, O. J. and Slagstad, D.: Modelling seasonal growth and composition of the kelp *Saccharina latissima*, *J. Appl. Phycol.*, 24, 759–776, <https://doi.org/10.1007/s10811-011-9695-y>, 2012.
- Brush, M. J. and Nixon, S. W.: Modeling the role of macroalgae in a shallow sub-estuary of Narragansett Bay, RI (USA), *Ecol. Modell.*, 221, 1065–1079, <https://doi.org/10.1016/j.ecolmodel.2009.11.002>, 2010.
- Buck, B. H. and Buchholz, C. M.: The offshore-ring: A new system design for the open ocean aquaculture of macroalgae, *J. Appl. Phycol.*, 660 16, 355–368, <https://doi.org/10.1023/B:JAPH.0000047947.96231.ea>, 2004.



- Buschmann, A. H., Camus, C., Infante, J., Neori, A., Israel, Á., Hernández-González, M. C., Pereda, S. V., Gomez-Pinchetti, J. L., Golberg, A., Tadmor-Shalev, N., and Critchley, A. T.: Seaweed production: overview of the global state of exploitation, farming and emerging research activity, *Eur. J. Phycol.*, 52, 391–406, <https://doi.org/10.1080/09670262.2017.1365175>, 2017.
- Carpenter, L. J. and Liss, P. S.: On temperate sources of bromoform and other reactive organic bromine gases, *J. Geophys. Res. Atmos.*, 105, 20 539–20 547, <https://doi.org/10.1029/2000JD900242>, 2000.
- Chen, H., Zhou, D., Luo, G., Zhang, S., and Chen, J.: Macroalgae for biofuels production: Progress and perspectives, *Renew. Sustain. Energy Rev.*, 47, 427–437, <https://doi.org/10.1016/j.rser.2015.03.086>, 2015.
- Chung, I. K., Beardall, J., Mehta, S., Sahoo, D., and Stojkovic, S.: Using marine macroalgae for carbon sequestration: A critical appraisal, *J. Appl. Phycol.*, 23, 877–886, <https://doi.org/10.1007/s10811-010-9604-9>, 2011.
- 670 Ciais, P., Sabine, C., Bala, G., Bopp, L., Brovkin, V., Canadell, J., Chhabra, A., DeFries, R., Galloway, J., Heimann, M., Jones, C., Quéré, C. L., Myneni, R., Piao, S., and Thornton, P.: Carbon and other biogeochemical cycles, in: *Clim. Chang. 2013 Phys. Sci. Basis Work. Gr. I Contrib. to Fifth Assess. Rep. Intergov. Panel Clim. Chang.*, edited by Intergovernmental Panel on Climate Change, vol. 9781107057, pp. 465–570, Cambridge University Press, Cambridge, <https://doi.org/10.1017/CBO9781107415324.015>, 2013.
- Conover, J., Green, L. A., and Thornber, C. S.: Biomass decay rates and tissue nutrient loss in bloom and non-bloom-forming macroalgal species, *Estuar. Coast. Shelf Sci.*, 178, 58–64, <https://doi.org/10.1016/j.ecss.2016.05.018>, 2016.
- 675 Daniel, J. S., Solomon, S., and Albritton, D. L.: On the evaluation of halocarbon radiative forcing and global warming potentials, *J. Geophys. Res.*, 100, 1271–1285, <https://doi.org/10.1029/94JD02516>, 1995.
- D’Auriac, M. A., Hancke, K., Gundersen, H., Frigstad, H., and Borgersen, G.: Blue Carbon eDNA - A novel eDNA method to trace macroalgae carbon in marine sediments, Tech. rep., Norwegian Institute for Water Research, 2021.
- 680 Dean, J., Kiendler-Scharr, A., Mengis, N., Rudich, Y., Schepanski, K., and Zimmermann, R.: Above us only sky, *Commun. Earth Environ.*, 2, 179, <https://doi.org/10.1038/s43247-021-00245-0>, 2021.
- Duarte, C. M., Wu, J., Xiao, X., Bruhn, A., and Krause-Jensen, D.: Can seaweed farming play a role in climate change mitigation and adaptation?, *Front. Mar. Sci.*, 4, <https://doi.org/10.3389/fmars.2017.00100>, 2017.
- Duarte, P. and Ferreira, J.: A model for the simulation of macroalgal population dynamics and productivity, *Ecol. Modell.*, 98, 199–214, [https://doi.org/10.1016/S0304-3800\(96\)01915-1](https://doi.org/10.1016/S0304-3800(96)01915-1), 1997.
- 685 Duarte, P., Meneses, R., Hawkins, A. J., Zhu, M., Fang, J., and Grant, J.: Mathematical modelling to assess the carrying capacity for multi-species culture within coastal waters, *Ecol. Modell.*, 168, 109–143, [https://doi.org/10.1016/S0304-3800\(03\)00205-9](https://doi.org/10.1016/S0304-3800(03)00205-9), 2003.
- Eby, M., Zickfeld, K., Montenegro, A., Archer, D., Meissner, K. J., and Weaver, A. J.: Lifetime of anthropogenic climate change: Millennial time scales of potential CO₂ and surface temperature perturbations, *J. Clim.*, 22, 2501–2511, <https://doi.org/10.1175/2008JCLI2554.1>, 2009.
- 690 Eby, M., Weaver, A. J., Alexander, K., Zickfeld, K., Abe-Ouchi, A., Cimadoribus, A. A., Crespin, E., Drijfhout, S. S., Edwards, N. R., Eliseev, A. V., Feulner, G., Fichfet, T., Forest, C. E., Goosse, H., Holden, P. B., Joos, F., Kawamiya, M., Kicklighter, D., Kienert, H., Matsumoto, K., Mokhov, I. I., Monier, E., Olsen, S. M., Pedersen, J. O., Perrette, M., Philippon-Berthier, G., Ridgwell, A., Schlosser, A., Von Deimling, T. S., Shaffer, G., Smith, R. S., Spahni, R., Sokolov, A. P., Steinacher, M., Tachiiri, K., Tokos, K., Yoshimori, M., Zeng, N., and Zhao, F.: Historical and idealized climate model experiments: An intercomparison of Earth system models of intermediate complexity, *Clim. Past*, 9, 1111–1140, <https://doi.org/10.5194/cp-9-1111-2013>, 2013.
- Edo, A., Hertwich, E., and Heeren, N.: Emissions Gap Report 2019, UNEP/Earthprint, Nairobi, <http://www.unenvironment.org/emissionsgap>, 2019.



- Eisaman, M. D., Parajuly, K., Tuganov, A., Eldershaw, C., Chang, N., and Littau, K. A.: CO₂ extraction from seawater using bipolar membrane electro dialysis, *Energy Environ. Sci.*, 5, 7346–7352, <https://doi.org/10.1039/c2ee03393c>, 2012.
- 700 Eriksson, B. K. and Bergström, L.: Local distribution patterns of macroalgae in relation to environmental variables in the northern Baltic Proper, *Estuar. Coast. Shelf Sci.*, 62, 109–117, <https://doi.org/10.1016/j.ecss.2004.08.009>, 2005.
- Fanning, A. F. and Weaver, A. J.: An atmospheric energy-moisture balance model: Climatology, interpentadal climate change, and coupling to an ocean general circulation model, *J. Geophys. Res. Atmos.*, 101, 15 111–15 128, <https://doi.org/10.1029/96jd01017>, 1996.
- 705 FAO: The State of World Fisheries and Aquaculture 2018-Meeting the sustainable development goals, 2018.
- Fernand, F., Israel, A., Skjermo, J., Wichard, T., Timmermans, K. R., and Golberg, A.: Offshore macroalgae biomass for bioenergy production: Environmental aspects, technological achievements and challenges, *Renew. Sustain. Energy Rev.*, 75, 35–45, <https://doi.org/10.1016/j.rser.2016.10.046>, 2017.
- Fogarty, M. C., Fewings, M. R., Paget, A. C., and Dierssen, H. M.: The Influence of a Sandy Substrate, Seagrass, or Highly Turbid Water on
710 Albedo and Surface Heat Flux, *J. Geophys. Res. Ocean.*, 123, 53–73, <https://doi.org/10.1002/2017JC013378>, 2018.
- Friedlingstein, P., Jones, M. W., O’Sullivan, M., Andrew, R. M., Bakker, D. C. E., Hauck, J., Le Quééré, C., Peters, G. P., Peters, W., Pongratz, J., Sitch, S., Canadell, J. G., Ciais, P., Jackson, R. B., Alin, S. R., Anthoni, P., Bates, N. R., Becker, M., Bellouin, N., Bopp, L., Chau, T. T., Chevallier, F., Chini, L. P., Cronin, M., Currie, K. I., Decharme, B., Djeutchouang, L., Dou, X., Evans, W., Feely, R. A., Feng, L., Gasser, T., Gilfillan, D., Gkritzalis, T., Grassi, G., Gregor, L., Gruber, N., Gürses, O., Harris, I., Houghton, R. A., Hurtt, G. C., Iida, Y.,
715 Ilyina, T., Lujikx, I. T., Jain, A. K., Jones, S. D., Kato, E., Kennedy, D., Klein Goldewijk, K., Knauer, J., Korsbakken, J. I., Körtzinger, A., Landschützer, P., Lauvset, S. K., Lefèvre, N., Lienert, S., Liu, J., Marland, G., McGuire, P. C., Melton, J. R., Munro, D. R., Nabel, J. E. M. S., Nakaoka, S.-I., Niwa, Y., Ono, T., Pierrot, D., Poulter, B., Rehder, G., Resplandy, L., Robertson, E., Rödenbeck, C., Rosan, T. M., Schwinger, J., Schwingshackl, C., Séférian, R., Sutton, A. J., Sweeney, C., Tanhua, T., Tans, P. P., Tian, H., Tilbrook, B., Tubiello, F., van der Werf, G., Vuichard, N., Wada, C., Wanninkhof, R., Watson, A., Willis, D., Wiltshire, A. J., Yuan, W., Yue, C., Yue, X., Zaehle, S.,
720 and Zeng, J.: Global Carbon Budget 2021, *Earth System Science Data Discussions*, 2021, 1–191, <https://doi.org/10.5194/essd-2021-386>, 2021.
- Froehlich, H. E., Afflerbach, J. C., Frazier, M., and Halpern, B. S.: Blue Growth Potential to Mitigate Climate Change through Seaweed Offsetting, *Curr. Biol.*, 29, 3087–3093.e3, <https://doi.org/10.1016/j.cub.2019.07.041>, 2019.
- Fuss, S., Canadell, J. G., Ciais, P., Jackson, R. B., Jones, C. D., Lyngfelt, A., Peters, G. P., and Van Vuuren, D. P.: Moving toward Net-Zero
725 Emissions Requires New Alliances for Carbon Dioxide Removal, *One Earth*, 3, 145–149, <https://doi.org/10.1016/j.oneear.2020.08.002>, 2020.
- Gao, G., Burgess, J. G., Wu, M., Wang, S., and Gao, K.: Using macroalgae as biofuel: Current opportunities and challenges, *Bot. Mar.*, 63, 355–370, <https://doi.org/10.1515/bot-2019-0065>, 2020.
- Gao, K. and McKinley, K. R.: Use of macroalgae for marine biomass production and CO₂ remediation: a review, *J. Appl. Phycol.*, 6, 45–60,
730 <https://doi.org/10.1007/BF02185904>, 1994.
- Garcia, H. E., Locarnini, R. A., Boyer, T. P., Antonov, J. I., Zweng, M. M., Baranova, O. K., and Johnson, D. R.: World Ocean Atlas 2009, Volume 4: Nutrients (phosphate, nitrate, and silicate), NOAA World Ocean Atlas, 71, 398, <http://www.nodc.noaa.gov/OC5/indprod.html>, 2010.
- Glaser, J. A.: Climate geoengineering, *Clean Technol. Environ. Policy*, 12, 91–95, <https://doi.org/10.1007/s10098-010-0287-3>, 2010.



- 735 Gruber, N., Clement, D., Carter, B. R., Feely, R. A., van Heuven, S., Hoppema, M., Ishii, M., Key, R. M., Kozyr, A., Lauvset, S. K., Monaco, C. L., Mathis, J. T., Murata, A., Olsen, A., Perez, F. F., Sabine, C. L., Tanhua, T., and Wanninkhof, R.: The oceanic sink for anthropogenic CO₂ from 1994 to 2007, *Science* (80-.), 363, 1193–1199, <https://doi.org/10.1126/science.aau5153>, 2019.
- Hadley, S., Wild-Allen, K., Johnson, C., and Macleod, C.: Modeling macroalgae growth and nutrient dynamics for integrated multi-trophic aquaculture, *J. Appl. Phycol.*, 27, 901–916, <https://doi.org/10.1007/s10811-014-0370-y>, 2015.
- 740 Heinze, C., Meyer, S., Goris, N., Anderson, L., Steinfeldt, R., Chang, N., Le Quéré, C., and Bakker, D. C.: The ocean carbon sink - Impacts, vulnerabilities and challenges, *Earth Syst. Dyn.*, 6, 327–358, <https://doi.org/10.5194/esd-6-327-2015>, 2015.
- IPCC: Summary for Policymakers, in: *Global Warming of 1.5°C. An IPCC Special Report on the impacts of global warming of 1.5°C above pre-industrial levels and related global greenhouse gas emission pathways, in the context of strengthening the global response to the threat of climate change.*, edited by Masson-Delmotte, V., Roberts, P. Z. H.-O. P. D., Skea, J., Shukla, P., Pirani, A., Moufouma-Okia, W., Péan, C., Pidcock, R., Connors, S., Matthews, J., Chen, Y., Zhou, X., Gomis, M., Lonnoy, E., Maycock, T., Tignor, M., and (eds.), T. W., pp. 17–20, World Meteorological Organization, Geneva, Switzerland, www.environmentalgraphiti.org, 2018.
- 745 Jiang, Z., Liu, J., Li, S., Chen, Y., Du, P., Zhu, Y., Liao, Y., Chen, Q., Shou, L., Yan, X., Zeng, J., and Chen, J.: Kelp cultivation effectively improves water quality and regulates phytoplankton community in a turbid, highly eutrophic bay, *Sci. Total Environ.*, 707, 135 561, <https://doi.org/10.1016/j.scitotenv.2019.135561>, 2020.
- 750 Keller, D. P., Oschlies, A., and Eby, M.: A new marine ecosystem model for the University of Victoria earth system climate model, *Geosci. Model Dev.*, 5, 1195–1220, <https://doi.org/10.5194/gmd-5-1195-2012>, 2012.
- Keller, D. P., Feng, E. Y., and Oschlies, A.: Potential climate engineering effectiveness and side effects during a high carbon dioxide-emission scenario, *Nat. Commun.*, 5, 3304, <https://doi.org/10.1038/ncomms4304>, 2014.
- Keller, D. P., Lenton, A., Littleton, E. W., Oschlies, A., Scott, V., and Vaughan, N. E.: The Effects of Carbon Dioxide Removal on the Carbon Cycle, *Curr. Clim. Chang. Reports*, 4, 250–265, <https://doi.org/10.1007/s40641-018-0104-3>, 2018.
- 755 Kim, J. K., Stekoll, M., and Yarish, C.: Opportunities, challenges and future directions of open-water seaweed aquaculture in the United States, *Phycologia*, 58, 446–461, <https://doi.org/10.1080/00318884.2019.1625611>, 2019.
- Kirk, J. T. O.: *Light and Photosynthesis in Aquatic Ecosystems*, Cambridge University Press, 2 edn., <https://doi.org/10.1017/CBO9780511623370>, 1994.
- 760 Koch, M., Bowes, G., Ross, C., and Zhang, X. H.: Climate change and ocean acidification effects on seagrasses and marine macroalgae, *Glob. Chang. Biol.*, 19, 103–132, <https://doi.org/10.1111/j.1365-2486.2012.02791.x>, 2013.
- Köhler, P., Abrams, J. F., Völker, C., Hauck, J., and Wolf-Gladrow, D. A.: Geoengineering impact of open ocean dissolution of olivine on atmospheric CO₂, surface ocean pH and marine biology, *Environ. Res. Lett.*, 8, <https://doi.org/10.1088/1748-9326/8/1/014009>, 2013.
- Krause-Jensen, D. and Duarte, C. M.: Substantial role of macroalgae in marine carbon sequestration, *Nat. Geosci.*, 9, 737–742, <https://doi.org/10.1038/ngeo2790>, 2016.
- 765 Kvale, K., Prowe, A. E., Chien, C. T., Landolfi, A., and Oschlies, A.: Zooplankton grazing of microplastic can accelerate global loss of ocean oxygen, *Nat. Commun.*, 12, <https://doi.org/10.1038/s41467-021-22554-w>, 2021.
- Kvale, K. F. and Meissner, K. J.: Primary production sensitivity to phytoplankton light attenuation parameter increases with transient forcing, *Biogeosciences*, 14, 4767–4780, <https://doi.org/10.5194/bg-14-4767-2017>, 2017.
- 770 Latumus, F.: Release of volatile halogenated organic compounds by unialgal cultures of polar macroalgae, *Chemosphere*, 31, 3387–3395, [https://doi.org/10.1016/0045-6535\(95\)00190-J](https://doi.org/10.1016/0045-6535(95)00190-J), 1995.



- Laurens, L. M., Lane, M., and Nelson, R. S.: Sustainable Seaweed Biotechnology Solutions for Carbon Capture, Composition, and Deconstruction, *Trends Biotechnol.*, 38, 1232–1244, <https://doi.org/10.1016/j.tibtech.2020.03.015>, 2020.
- 775 Lawrence, M. G., Schäfer, S., Muri, H., Scott, V., Oschlies, A., Vaughan, N. E., Boucher, O., Schmidt, H., Haywood, J., and Scheffran, J.: Evaluating climate geoengineering proposals in the context of the Paris Agreement temperature goals, *Nat. Commun.*, 9, <https://doi.org/10.1038/s41467-018-05938-3>, 2018.
- Leedham, E. C., Hughes, C., Keng, F. S., Phang, S. M., Malin, G., and Sturges, W. T.: Emission of atmospherically significant halocarbons by naturally occurring and farmed tropical macroalgae, *Biogeosciences*, 10, 3615–3633, <https://doi.org/10.5194/bg-10-3615-2013>, 2013.
- 780 Lehahn, Y., Ingle, K. N., and Golberg, A.: Global potential of offshore and shallow waters macroalgal biorefineries to provide for food, chemicals and energy: feasibility and sustainability, *Algal Res.*, 17, 150–160, <https://doi.org/10.1016/j.algal.2016.03.031>, 2016.
- Liu, Z. and Huguenard, K.: Hydrodynamic Response of a Floating Aquaculture Farm in a Low Inflow Estuary, *J. Geophys. Res. Ocean.*, 125, 0–3, <https://doi.org/10.1029/2019JC015625>, 2020.
- Luo, M., Gieskes, J., Chen, L., Scholten, J., Pan, B., Lin, G., and Chen, D.: Sources, Degradation, and Transport of Organic Matter in the New Britain Shelf-Trench Continuum, Papua New Guinea, *J. Geophys. Res. Biogeosciences*, 124, 1680–1695, <https://doi.org/10.1029/2018JG004691>, 2019.
- 785 Macreadie, P. I., Serrano, O., Maher, D. T., Duarte, C. M., and Beardall, J.: Addressing calcium carbonate cycling in blue carbon accounting, *Limnol. Oceanogr. Lett.*, 2, 195–201, <https://doi.org/10.1002/lol2.10052>, 2017.
- Macreadie, P. I., Anton, A., Raven, J. A., Beaumont, N., Connolly, R. M., Friess, D. A., Kelleway, J. J., Kennedy, H., Kuwae, T., Lavery, P. S., Lovelock, C. E., Smale, D. A., Apostolaki, E. T., Atwood, T. B., Baldock, J., Bianchi, T. S., Chmura, G. L., Eyre, B. D., Fourqurean, J. W., Hall-Spencer, J. M., Huxham, M., Hendriks, I. E., Krause-Jensen, D., Laffoley, D., Luisetti, T., Marbà, N., Masque, P., McGlathery, K. J., Megonigal, J. P., Murdiyarsa, D., Russell, B. D., Santos, R., Serrano, O., Silliman, B. R., Watanabe, K., and Duarte, C. M.: The future of Blue Carbon science, *Nat. Commun.*, 10, 1–13, <https://doi.org/10.1038/s41467-019-11693-w>, 2019.
- 790 Martin, T., Park, W., and Latif, M.: Multi-centennial variability controlled by Southern Ocean convection in the Kiel Climate Model, *Clim. Dyn.*, 40, 2005–2022, <https://doi.org/10.1007/s00382-012-1586-7>, 2013.
- 795 Martins, I. and Marques, J. C.: A model for the growth of opportunistic macroalgae (*Enteromorpha* sp.) in tidal estuaries, *Estuar. Coast. Shelf Sci.*, 55, 247–257, <https://doi.org/10.1006/ecss.2001.0900>, 2002.
- Matear, R. J. and Elliott, B.: Enhancement of oceanic uptake of anthropogenic CO₂ by macronutrient fertilization, *J. Geophys. Res. C Ocean.*, 109, 1–14, <https://doi.org/10.1029/2000JC000321>, 2004.
- 800 Meinshausen, M., Smith, S. J., Calvin, K., Daniel, J. S., Kainuma, M. L., Lamarque, J., Matsumoto, K., Montzka, S. A., Raper, S. C., Riahi, K., Thomson, A., Velders, G. J., and van Vuuren, D. P.: The RCP greenhouse gas concentrations and their extensions from 1765 to 2300, *Clim. Change*, 109, 213–241, <https://doi.org/10.1007/s10584-011-0156-z>, 2011.
- Meissner, K. J., Weaver, A. J., Matthews, H. D., and Cox, P. M.: The role of land surface dynamics in glacial inception: A study with the UVic Earth System Model, *Clim. Dyn.*, 21, 515–537, <https://doi.org/10.1007/s00382-003-0352-2>, 2003.
- Mengis, N., Martin, T., Keller, D. P., and Oschlies, A.: Assessing climate impacts and risks of ocean albedo modification in the Arctic, *J. Geophys. Res. Ocean.*, 121, 3044–3057, <https://doi.org/10.1002/2015JC011433>, 2016.
- 805 Minx, J. C., Lamb, W. F., Callaghan, M. W., Bornmann, L., and Fuss, S.: Fast growing research on negative emissions, *Environ. Res. Lett.*, 12, <https://doi.org/10.1088/1748-9326/aa5ee5>, 2017.



- Navarrete, I. A., Kim, D. Y., Wilcox, C., Reed, D. C., Ginsburg, D. W., Dutton, J. M., Heidelberg, J., Raut, Y., and Wilcox, B. H.: Effects of depth-cycling on nutrient uptake and biomass production in the giant kelp *Macrocystis pyrifera*, *Renew. Sustain. Energy Rev.*, 141, 110 747, <https://doi.org/10.1016/j.rser.2021.110747>, 2021.
- Nepf, H. M.: Hydrodynamics of vegetated channels, *J. Hydraul. Res.*, 50, 262–279, <https://doi.org/10.1080/00221686.2012.696559>, 2012.
- N'Yeurt, A. D. R., Chynoweth, D. P., Capron, M. E., Stewart, J. R., and Hasan, M. A.: Negative carbon via ocean afforestation, *Process Saf. Environ. Prot.*, 90, 467–474, <https://doi.org/10.1016/j.psep.2012.10.008>, 2012.
- Orr, J., Najjar, R., Sabine, C., and Joos, F.: Abiotic-howto, Intern. OCMIP Report, LSCE/CEA Saclay, Gifsur-Yvette, Fr., 1999, 1–29, <http://www.cgd.ucar.edu/oce/klindsay/OCMIP/HOWTO-Abiotic.pdf>, 1999.
- Orr, J. C. and Sarmiento, J. L.: Potential of marine macroalgae as a sink for CO₂: Constraints from a 3-D general circulation model of the global ocean, *Water, Air, Soil Pollut.*, 64, 405–421, <https://doi.org/10.1007/BF00477113>, 1992.
- Oschlies, A.: A committed fourfold increase in ocean oxygen loss, *Nat. Commun.*, 12, 2307, <https://doi.org/10.1038/s41467-021-22584-4>, 2021.
- Oschlies, A., Pahlow, M., Yool, A., and Matear, R. J.: Climate engineering by artificial ocean upwelling: Channelling the sorcerer's apprentice, *Geophys. Res. Lett.*, 37, 1–5, <https://doi.org/10.1029/2009GL041961>, 2010.
- Oschlies, A., Koeve, W., Landolfi, A., and Kähler, P.: Loss of fixed nitrogen causes net oxygen gain in a warmer future ocean, *Nat. Commun.*, 10, 1–7, <https://doi.org/10.1038/s41467-019-10813-w>, 2019.
- Oyinlola, M. A., Reygondeau, G., Wabnitz, C. C., and Cheung, W. W.: Projecting global mariculture diversity under climate change, *Glob. Chang. Biol.*, 26, 2134–2148, <https://doi.org/10.1111/gcb.14974>, 2020.
- Pacanowski, R.: MOM 2 Version 2.0 (beta) Documentation User's Guide and Reference Manual, Model Manual, 0, 1996.
- Partanen, A. I., Keller, D. P., Korhonen, H., and Matthews, H. D.: Impacts of sea spray geoengineering on ocean biogeochemistry, *Geophys. Res. Lett.*, 43, 7600–7608, <https://doi.org/10.1002/2016GL070111>, 2016.
- Peteiro, C., Sánchez, N., Dueñas-Liaño, C., and Martínez, B.: Open-sea cultivation by transplanting young fronds of the kelp *Saccharina latissima*, *J. Appl. Phycol.*, 26, 519–528, <https://doi.org/10.1007/s10811-013-0096-2>, 2014.
- Peters, G. P., Andrew, R. M., Boden, T., Canadell, J. G., Ciais, P., Le Quéré, C., Marland, G., Raupach, M. R., and Wilson, C.: The challenge to keep global warming below 2C, *Nat. Clim. Chang.*, 3, 4–6, <https://doi.org/10.1038/nclimate1783>, 2013.
- Ramaswamy, V., Schwarzkopf, M. D., and Shine, K. P.: Radiative forcing of climate from halocarbon-induced global stratospheric ozone loss, *Nature*, 355, 810–812, <https://doi.org/10.1038/355810a0>, 1992.
- Raven, J.: Blue carbon: Past, present and future, with emphasis on macroalgae, *Biol. Lett.*, 14, 20180336, <https://doi.org/10.1098/rsbl.2018.0336>, 2018.
- Ravishankara, A. R., Daniel, J. S., and Portmann, R. W.: Nitrous oxide (N₂O): The dominant ozone-depleting substance emitted in the 21st century, *Science (80-.)*, 326, 123–125, <https://doi.org/10.1126/science.1176985>, 2009.
- Reith, F., Keller, D. P., and Oschlies, A.: Revisiting ocean carbon sequestration by direct injection: A global carbon budget perspective, *Earth Syst. Dyn.*, 7, 797–812, <https://doi.org/10.5194/esd-7-797-2016>, 2016.
- Roberts, D. A., Paul, N. A., Dworjanyn, S. A., Bird, M. I., and De Nys, R.: Biochar from commercially cultivated seaweed for soil amelioration, *Sci. Rep.*, 5, 1–6, <https://doi.org/10.1038/srep09665>, 2015.
- Robinson, J., Popova, E. E., Yool, A., Srokosz, M., Lampitt, R. S., and Blundell, J. R.: How deep is deep enough? Ocean iron fertilization and carbon sequestration in the Southern Ocean, *Geophys. Res. Lett.*, 41, 2489–2495, <https://doi.org/10.1002/2013GL058799>, 2014.



- 845 Rogelj, J., Popp, A., Calvin, K. V., Luderer, G., Emmerling, J., Gernaat, D., Fujimori, S., Strefler, J., Hasegawa, T., Marangoni, G., Krey, V., Kriegler, E., Riahi, K., van Vuuren, D. P., Doelman, J., Drouet, L., Edmonds, J., Fricko, O., Harmsen, M., Havlík, P., Humpenöder, F., Stehfest, E., and Tavoni, M.: Scenarios towards limiting global mean temperature increase below 1.5 °C, *Nat. Clim. Chang.*, 8, 325–332, <https://doi.org/10.1038/s41558-018-0091-3>, 2018.
- Schmittner, A., Oschlies, A., Giraud, X., Eby, M., and Simmons, H. L.: A global model of the marine ecosystem for long-term simulations: Sensitivity to ocean mixing, buoyancy forcing, particle sinking, and dissolved organic matter cycling, *Global Biogeochem. Cycles*, 19, 1–17, <https://doi.org/10.1029/2004GB002283>, 2005.
- Schmittner, A., Oschlies, A., Matthews, H. D., and Galbraith, E. D.: Future changes in climate, ocean circulation, ecosystems, and biogeochemical cycling simulated for a business-as-usual CO₂ emission scenario until year 4000 AD, *Global Biogeochem. Cycles*, 22, 1–21, <https://doi.org/10.1029/2007GB002953>, 2008.
- 855 Scott, V., Haszeldine, R. S., Tett, S. F., and Oschlies, A.: Fossil fuels in a trillion tonne world, *Nat. Clim. Chang.*, 5, 419–423, <https://doi.org/10.1038/nclimate2578>, 2015.
- Sherman, M. T., Blaylock, R., Lucas, K., Capron, M. E., Stewart, J. R., DiMarco, S. F., Thyng, K., Hetland, R., Kim, M., Sullivan, C., Moscicki, Z., Tsukrov, I., Swift, M. R., Chambers, M. D., James, S. C., Brooks, M., Von Herzen, B., Jones, A., and Piper, D.: SeaweedPaddock: Initial Modeling and Design for a Sargassum Ranch, in: *Ocean. 2018 MTS/IEEE Charleston*, Ocean 2018, pp. 1–6, IEEE, <https://doi.org/10.1109/OCEANS.2018.8604848>, 2019.
- 860 Sichert, A., Corzett, C. H., Schechter, M. S., Unfried, F., Markert, S., Becher, D., Fernandez-Guerra, A., Liebeke, M., Schweder, T., Polz, M. F., and Hehemann, J. H.: Verrucomicrobia use hundreds of enzymes to digest the algal polysaccharide fucoidan, *Nat. Microbiol.*, 5, 1026–1039, <https://doi.org/10.1038/s41564-020-0720-2>, 2020.
- Smetacek, V., Klaas, C., Strass, V. H., Assmy, P., Montresor, M., Cisewski, B., Savoye, N., Webb, A., D’Ovidio, F., Arrieta, J. M., Bathmann, U., Bellerby, R., Berg, G. M., Croot, P., Gonzalez, S., Henjes, J., Herndl, G. J., Hoffmann, L. J., Leach, H., Losch, M., Mills, M. M., Neill, C., Peeken, I., Röttgers, R., Sachs, O., Sauter, E., Schmidt, M. M., Schwarz, J., Terbrüggen, A., and Wolf-Gladrow, D.: Deep carbon export from a Southern Ocean iron-fertilized diatom bloom, *Nature*, 487, 313–319, <https://doi.org/10.1038/nature11229>, 2012.
- Talley, L. D.: Closure of the global overturning circulation through the Indian, Pacific, and southern oceans, *Oceanography*, 26, 80–97, <https://doi.org/10.5670/oceanog.2013.07>, 2013.
- 870 Taylor, L. L., Quirk, J., Thorley, R. M., Kharecha, P. A., Hansen, J., Ridgwell, A., Lomas, M. R., Banwart, S. A., and Beerling, D. J.: Enhanced weathering strategies for stabilizing climate and averting ocean acidification, *Nat. Clim. Chang.*, 6, 402–406, <https://doi.org/10.1038/nclimate2882>, 2016.
- Tegtmeier, S., Krüger, K., Quack, B., Atlas, E. L., Pisso, I., Stohl, A., and Yang, X.: Emission and transport of bromocarbons: From the West Pacific ocean into the stratosphere, *Atmos. Chem. Phys.*, 12, 10633–10648, <https://doi.org/10.5194/acp-12-10633-2012>, 2012.
- 875 Tegtmeier, S., Quack, B., Atlas, E., Blake, D. R., Engel, A., Hepach, H., Hossaini, R., Navarro, M. A., Raimund, S., Sala, S., Shi, Q., and Ziska, F.: The contribution of oceanic methyl iodide to stratospheric iodine, *Atmos. Chem. Phys. Discuss.*, 13, 11427–11471, <https://doi.org/10.5194/acpd-13-11427-2013>, 2013.
- Thomas, R. E. and McLelland, S. J.: The impact of macroalgae on mean and turbulent flow fields, *J. Hydrodyn.*, 27, 427–435, [https://doi.org/10.1016/S1001-6058\(15\)60500-5](https://doi.org/10.1016/S1001-6058(15)60500-5), 2015.
- 880 Thomas, S.: Blue carbon: Knowledge gaps, critical issues, and novel approaches, *Ecol. Econ.*, 107, 22–38, <https://doi.org/10.1016/j.ecolecon.2014.07.028>, 2014.



- Trancoso, A. R., Saraiva, S., Fernandes, L., Pina, P., Leitão, P., and Neves, R.: Modelling macroalgae using a 3D hydrodynamic-ecological model in a shallow, temperate estuary, *Ecol. Modell.*, 187, 232–246, <https://doi.org/10.1016/j.ecolmodel.2005.01.054>, 2005.
- 885 Trevathan-Tackett, S. M., Kelleway, J., Macreadie, P. I., Beardall, J., Ralph, P., and Bellgrove, A.: Comparison of marine macrophytes for their contributions to blue carbon sequestration, *Ecology*, 96, 3043–3057, <https://doi.org/10.1890/15-0149.1>, 2015.
- UNFCCC, V.: Adoption of the Paris agreement, United Nations Office at Geneva, Geneva Google Scholar, 2015.
- Van Der Molen, J., Ruardij, P., Mooney, K., Kerrison, P., O'Connor, N., Gorman, E., Timmermans, K., Wright, S., Kelly, M., Hughes, A. D., Capuzzo, E., O'Connor, N. E., Gorman, E., Timmermans, K., Wright, S., Kelly, M., Hughes, A. D., Capuzzo, E., O'Connor, N., Gorman, E., Timmermans, K., Wright, S., Kelly, M., Hughes, A. D., Capuzzo, E., O'Connor, N. E., Gorman, E., Timmermans, K., Wright, S., Kelly, M., Hughes, A. D., and Capuzzo, E.: Modelling potential production and environmental effects of macroalgae farms in UK and Dutch coastal waters, *Biogeosciences Discuss.*, 15, 1–43, <https://doi.org/10.5194/bg-15-1123-2018>, 2017.
- 890 Weaver, A. J., Eby, M., Wiebe, E. C., Bitz, C. M., Duffy, P. B., Ewen, T. L., Fanning, A. F., Holland, M. M., MacFadyen, A., Matthews, H. D., Meissner, K. J., Saenko, O., Schmittner, A., Wang, H., and Yoshimori, M.: The UVic earth system climate model: Model description, climatology, and applications to past, present and future climates, *Atmosphere-Ocean*, 39, 361–428, <https://doi.org/10.1080/07055900.2001.9649686>, 2001.
- 905 Weber, T. and Bianchi, D.: Efficient Particle Transfer to Depth in Oxygen Minimum Zones of the Pacific and Indian Oceans, *Front. Earth Sci.*, 8, 1–11, <https://doi.org/10.3389/feart.2020.00376>, 2020.
- Yokoyama, S., Jonouchi, K., and Imou, K.: Energy Production from Marine Biomass : Fuel Cell Power Generation Driven by Methane Produced from Seaweed, *Eng. Technol.*, 22, 320–323, <http://www.waset.org/journals/waset/v28.php>, 2007.
- 900 Zhang, D., Yan, M., Niu, Y., Liu, X., van Zwieten, L., Chen, D., Bian, R., Cheng, K., Li, L., Joseph, S., Zheng, J., Zhang, X., Zheng, J., Crowley, D., Filley, T. R., and Pan, G.: Is current biochar research addressing global soil constraints for sustainable agriculture?, *Agric. Ecosyst. Environ.*, 226, 25–32, <https://doi.org/10.1016/j.agee.2016.04.010>, 2016.
- 905 Ziska, F., Quack, B., Abrahamsson, K., Archer, S. D., Atlas, E., Bell, T., Butler, J. H., Carpenter, L. J., Jones, C. E., Harris, N. R., Hepach, H., Heumann, K. G., Hughes, C., Kuss, J., Krüger, K., Liss, P., Moore, R. M., Orlikowska, A., Raimund, S., Reeves, C. E., Reifenhäuser, W., Robinson, A. D., Schall, C., Tanhua, T., Tegtmeier, S., Turner, S., Wang, L., Wallace, D., Williams, J., Yamamoto, H., Yvon-Lewis, S., and Yokouchi, Y.: Global sea-to-air flux climatology for bromoform, dibromomethane and methyl iodide, *Atmos. Chem. Phys.*, 13, 8915–8934, <https://doi.org/10.5194/acp-13-8915-2013>, 2013.